学位論文

Low Dimensional Electronic Behavior in Bi Anti-dot Thin Films

(Biアンチドット薄膜における低次元電子状態に関する研究)

平成２５年１２月博士（理学）申請

東京大学大学院理学系研究科化学専攻

パク　ヨンオク
朴　瑛玉

Low Dimensional Electronic Behavior in Bi Anti-dot Thin Films

by

Youngok Park

Department of Chemistry

Graduate School of Science

The University of Tokyo

December, 2013

Abstract

Low dimensional systems show fascinating physical properties including weak localization, being an example of Quantum confinement effects (QCE), and enhanced surface effects. Recent progress on nanotechnologies to fabricate and characterize nanostructures enabled to study peculiar properties unique to the low dimensional systems. The physical properties of low dimensional systems are highly dependent on temperature, external magnetic field and sizes of nanostructures relative to the Fermi wavelength and/or carrier mean free path, because the electron propagation path and electron scattering phenomena, including electron-electron scattering and electron-phonon scattering, are largely affected by these conditions.

Bismuth (Bi) has unique physical properties such as small effective mass, low carrier density, and long carrier mean free path as well as anisotropic Fermi surface. Furthermore, long Fermi wavelength (λ_F) of ~40 nm, originating from the unique shape of the Fermi surface, and small effective mass with low carrier density allow to study QCE in Bi nanostructures using a probe of magnetoresistance (MR).

In this thesis, I fabricated Bi anti-dot thin films on ordered porous alumina array templates by thermal evaporation technique. In order to study QCE of Bi anti-dot thin films, pore wall widths (w_{Bi}) and thickness of films (t) were systemically tailored relative to λ_F=~40 nm, which is a critical length parameter that restrict the motion of conduction carriers. Magneto-transport properties were measured as function of external magnetic field at several temperature regimes. The dimensionality was evaluated from the magneto-resistance data by using the Hikami-Larkin-Nagaoka model. As a consequence, I have found that the dimensionality of the

Bi anti-dot films changes from 1D-2D to 2D-3D with increasing w_{Bi} and t. Particularly, the 1D character appeared only when w_{Bi} is shorter than the coherence length and w_{Bi}, $t < \lambda_F$.

The behavior of electron and hole carriers as influenced by the size of anti-dot structure and temperature was analyzed in detail by assuming the two-band model. As a result, the density of electron carriers was found to be enhanced with decreasing the film thickness, indicating that the surface carriers were dominated by electrons. In the thinnest films with t = 25 nm, the hole density was significantly increased with w_{Bi}, which might reflect the increase of dimensionality.

Acknowledgements

For three and a half years at University of Tokyo, I had a wonderful time with many talented, enthusiastic and kind people, and I feel very happy to mention them here.

Above all, I would like to thank my supervisor Hasegawa-sensei who has been an excellent advisor to me. Not only did he give me a great opportunity to study in his group, but also he has always been a full of inspiration to me with his broad knowledge and astonishing capability.

I am grateful to Hirose-san for his support and guidance on the both experiments and theoretical work, and also to Fukumura-sensei and Nakao-san for their constant and passionate assistances. I appreciate Chikamatsu-san; his kind words of encouragement have enlightened me to proceed whenever I was feeling exhausted and frustrated.

I feel very fortunate to have studied with D.Oka-san, Ikemiya-san, Yang-san, Okazaki-san and Watanabe-san who were extremely kind to me.

Plus I would like to thank all the people who have supported me and cheered me up; Ohno-san, Mohri-san, Taira-san, Tsuruhama-san, Huong-san, Shimamoto-san, Matsuyama-san, Kihira-san, Sano-san, Takahashi-san, Noguchi-san, Inoue-san, Ukita-san, Aizawa-san, Shen-san, Suzuki-san, Yamazaki-san, M.Oka-san, Otaki-san, Kamisaka-san, Ohtsuka-san, Ogawa-san, Shigematsu-san, Kojima-san, Wei-san, Katayama-san, Krasienapibal-san, Kurita-san, Sei-san, Takaki-san, Ohnozuka-san, Kaminaga-san, Yamatake-san, Motaneeyachart-san, Yutaka-san, Keisuke-san, Kurauchi-san, Takeda-san, Imoji-san, Umino-san, Kikuci-san, Komazawa-san;

{Aaron Larocque, Gustavo Fernandes, Jinho Kim, Lyuba Kuznetsova, Prof. Xu} at Brown University; and Stephen Dempsey, Xingxing, Ohnishi-san, Keiko-san, Takako-san.

At Last, I would like to thank my parents, sister and grandparents for their endless love.

博士課程において充実した研究生活を送る事ができ、この非常に素晴らしい日々を忘れることはありません。多くのご指導やご助力を頂いた皆様に深く感謝いたします。

16th January 2014

in University of Tokyo

Youngok Park

Contents

List of Figures

Chapter 1

Introduction

1.1 Motivation and Outline of thesis

In this thesis,I have investigated quantum confinement effect of Bi anti-dot thin films with tailored pore wall widths as shown in Figure 1.1, where the regularly arranged pore walls can spatially restrict the paths of carriers.

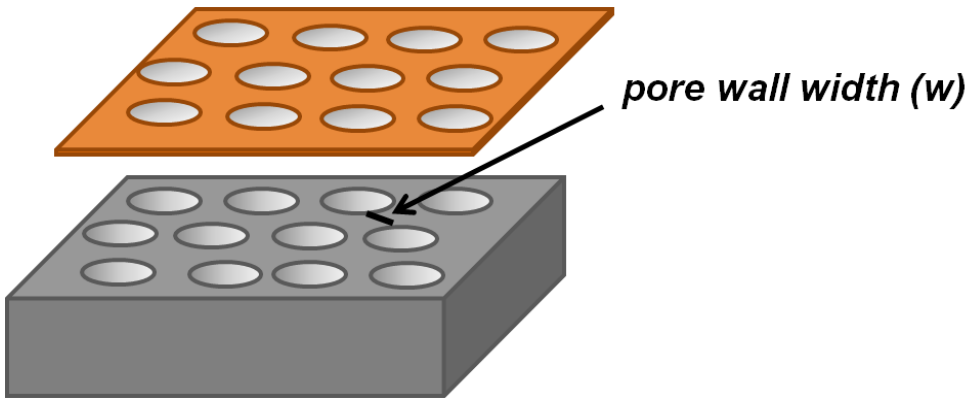

Figure 1.1.Schematic illustration of anti-dot thin films

Most of the previous related works have focused on Bi nanowires and thin films [1-4]. In thin films, electron systems are either two-dimensional or three-dimensional, depending on the film thickness. Thin nanowires can be one-dimensional. But the nanowire samples obtained so far are assemblies of many nanowires with random orientation so that it is hard to evaluate the transport properties low-dimensional electrons. Bi anti-dot thin films [5] are fascinating subjects of researches, in which distinctive physical properties such as low dimensional electron propagation are controllable by pore wall width and film thickness. Furthermore, in anti-dot thin films, the paths of low dimensional electrons are well restricted, which enables to characterize the anisotropic transport properties, including magneto-resistance, in a well-defined manner. In this thesis, Bi anti-dot thin films were fabricated on ordered porous alumina templates. The dimensionality of the anti-dot Bi thin films was deduced based on detailed analyses of the magneto-resistance data as a function of external magnetic field.

1.2 Quantum confinement effects

In low dimensional systems, such as nanostructures whose sizes are smaller than the Fermi wavelength and carrier mean free path, Quantum Confinement Effects (QCE) manifests itself as discrete energy band [6], confined charge carriers [7] and weak localization [4], which are not seen in bulk or three-dimensional system.

1.2.1 Density of states

Density of states (DOS) [8, 9] is the number of electronic states per unit volume in *k* space, which is described by

$$\rho(E) = \frac{dn(E)}{dE} \tag{1.1}$$

The total energy $E_n(k)$ in the *n*th band has the form,

$$E_n(k) = E_n + \frac{\hbar^2 k^2}{2}\left(\frac{1}{m_e} + \frac{1}{m_h}\right) \tag{1.2}$$

as function of momentum $\hbar k$ in the *k* space, wherem_e is the electron effective mass and $m_h$is the hole effective mass.

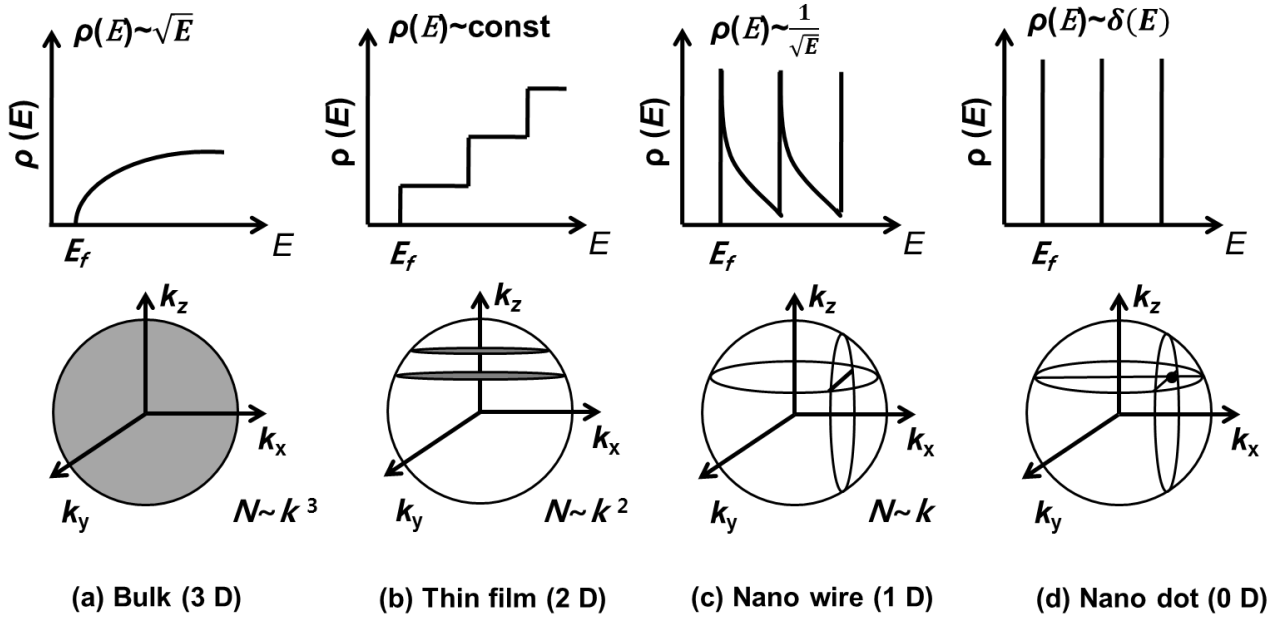

Figure1.2 Density of state as a function of energy for (a) bulk, (b) thin film, (c) nanowire and (d) nanodot.

In case of bulk, the volume in *k*-space is spherical,

$$V_k = \frac{4}{3}\pi k^3$$

$$k = \sqrt{k_x^2 + k_y^2 + k_z^2}$$

The volume per state is

$$V_{state} = k_x k_y k_z = \frac{8\pi^3}{L_x L_y L_z}$$

The number of states is

$$N_1 = \frac{V_k}{V_{state}} = \frac{k^3}{6\pi^2} L_x L_y L_z$$

Because of the spin degeneracy, the total number of states is

$$N = 2 \times N_1 = \frac{k^3}{3\pi^2} L_x L_y L_z$$

Therefore, the volume density is given by

$$\rho = \frac{N}{L_x L_y L_z} = \frac{k^3}{3\pi^2} \tag{1.3}$$

From Equations (1.2) and (1.3), the bulk density of state is derived as

$$\rho(E) = \frac{dn(E)}{dE} = \frac{1}{2\pi^2}\left(\frac{2\mu}{\hbar^2}\right)^{3/2}\sqrt{E - E_n}$$

where $\frac{1}{\mu} = \frac{1}{m_e} + \frac{1}{m_h}$.

As shown in Figure 1.2 (a), DOS of bulk has a parabolic shape with *E* ($\rho(E) \approx \sqrt{E}$). The change in DOS is very small in the vicinity of the Fermi level.

The DOS profile of two-dimensional thin film can be obtained by the same procedure. In thin films, electrons occupies a circular area in the *k*-space

$$A_k = \pi k^2$$

also

$$A_{state} = k_x k_y$$

where

$$k_x = \frac{2\pi}{L_x} \; and \; k_y = \frac{2\pi}{L_y}$$

Along the same way with bulk, DOS for thin film is expressed as

$$\rho(E) = \frac{\mu}{\pi\hbar^2}(E - E_n)$$

The DOS profile shows stepwise increases, as shown in Figure 1.2 (b).

Similarly, DOS for one-dimensional nanowire is described as

$$\rho(E) = \frac{1}{\pi}\sqrt{\frac{2\mu}{\hbar^2}}\sum \frac{1}{\sqrt{E - E_n}}$$

which is approximated by $\rho(E) \approx \frac{1}{\sqrt{E}}$, as shown in Figure 1.2 (c).

In nanodot case, DOS can be derived as

$$\rho(E) = 2\sum \delta(E - E_n)$$

This equation leads to infinitely narrow peaks, as illustrated in Figure 1.2 (d).

As described above, dimensionality significantly modifies DOS and such modification of DOS can provide unique electronic properties. For example, in low dimensional systems, the density of states near the Fermi level is increased, which can enhance the thermoelectric power, as demonstrated in Bi thin films [10-12]. It is also proposed that discrete energy levels cause semimetal to semiconductor transition, as reported in Bi thin films or nanowires [13-15].

1.2.2 Weak localization

Electron propagation plays a key role in carrier transport in electronic systems. Since the electronic behavior changes from ballistic to diffusive by decreasing the dimension of nanostructure [16, 17], weak localization phenomena, being one of the quantum confinement effects, appear in low dimensional systems. Especially, elastic scattering (electron-electron scattering) become dominant instated of inelastic scattering (electron-phonon scattering) at low temperature [18, 19]. Therefore, resistivity is decreased with decreasing temperature until a certain temperature, below which resistivity is suddenly increased the resistivity, as referred to as weak localization [19-21]. The diffusive electron motion in low dimensional systems at low

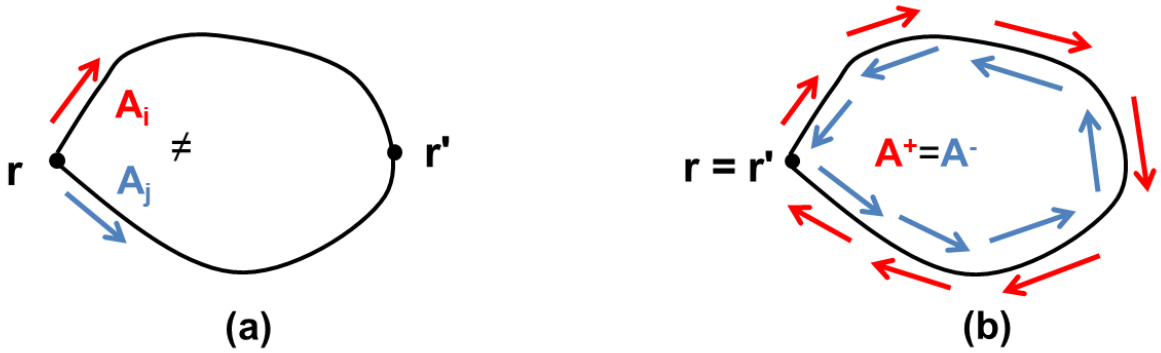

Figure 1.3.Examples of Feynman path accounting for the mechanism of coherent back scattering. Electron propagation in (a) classical regime and (b) low dimensional one which has time-reversal diffusive paths.

temperature results in coherence backscattering [19-22]. This phenomenon can be explained by Feynman path in Figure 1.3 [23].

In classical systems (Figure 1.3 (a)), electrons travel along different paths between two points. Whereas, electrons move in the two exactly same closed loops with opposite directions of motion, when electrons are confined in low dimensional systems (Figure 1.3 (b)). The total probability of electron propagation from *r* to *r*' in a time *t* is given by

$$P(r,r',t) = |\sum_i A_i|^2 = \sum_i |A_i|^2 + \sum_{i \neq j} A_i A_j^* \qquad (1.4)$$

whereA_i is the probability of electron propagation along the path *i*. The first term on the right side in Equation 1.4 is a correction for classical diffusion probability and second term describes quantum interference. If the start point (*r*) and end point (*r*') are different, the second term is corrected. In case that the starting and end points are same (*r* = *r*'), which causes coherent backscattering with time-reversal pairs, the probability amplitudes A^+ and A^- are equal to A.

This behavior results in twice larger probability than that of classical case, because$|A^+ + A^-|^2 = 4|A|^2$increases the probability of electron returns. Therefore resistivity is increased and the weak localization is manifested in low dimensional systems. The electron propagation in a closed loop is characterized by the phase coherence length (L_ϕ), which isa function of temperature, and the size of loop. L_ϕ is given by

$$L_\emptyset = \sqrt{D\tau_\emptyset} \tag{1.5}$$

where D is the diffusion constant and $\tau_\emptyset$ is the phase breaking time. The inelastic scattering is in inverse proportion to $\tau_\emptyset$. Consequently, L_ϕ is larger at low temperature where inelastic scattering is suppressed [24, 25].

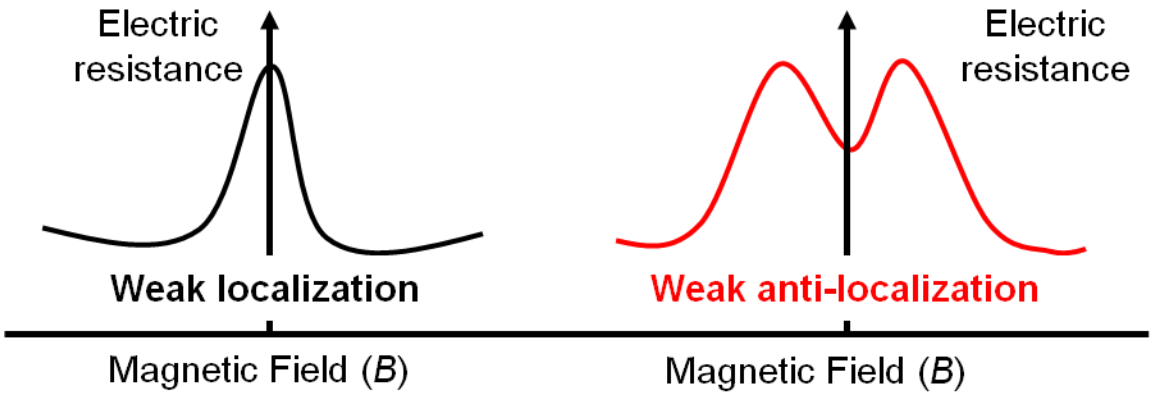

Figure 1.4 Magnetoresistance behavior in (a) weakly localized and (b) weakly anti-localized electron systems

1.2.3 Weak anti-localization

The time-reversal two paths in the same loop are destroyed by strong spin-orbit coupling which decreases the probability of back scattering. The destroyed interference of two wave functions results in lowered resistivity in the vicinity of zero magnetic fields at low temperature, as shown in Figure 1.4 [26-28]. This phenomenon enhances the conductivity, contrary to weak localization, and called weak anti-localization.

When the weak localization effects is taken into account, the conductivity associated with electron diffusive propagation in two dimensional systems is corrected by

$$\Delta\sigma \approx -2\frac{e^2}{\hbar}\ln\left(\frac{L_\emptyset}{l}\right)$$

where$l$ is the mean free path. As mentioned above, L_ϕ is temperature dependent and, therefore, conductivity also shows logarithmic temperature dependence in disordered low dimensional systems at low temperature under low magnetic field. In addition, the weak localization effect enhances electron-electron interaction, particularly the interaction with neighbor electrons [29]. Therefore, the electrons diffusive propagation is confined in a limited range. As a consequence of weak localization or weak anti-localization effects, electron propagation properties in low dimensional system are substantially modified.

1.3 Bismuth

Bulk Bi is a semimetal with rhombohedra structure [30], in which the conduction and valence bands overlap in energy at *L*-point and *T*-point, respectively. Bi also has distinctive physical properties, such as low carrier density, which is 4−5 orders of magnitude smaller than those of most metals, small electron effective mass of about $0.001m_e$ [31], and long carrier mean free path of ~100 nm at 300 K and ~400 μm at 4 K [32]. Furthermore, long Fermi wavelength (λ_F) of ~40 nm [33], originating from the unique shape of the Fermi surface, and small effective mass with low carrier density allow to study QCE in Bi nanostructures [34, 35] and to observed large magnetoresistance (MR) [36]. For example, Bi thin films and nanowires, whose sizes are smaller than or comparable to λ_F, show various size effects on their transport properties, including semimetal-to-semiconductor transition [13-15] and enhanced weak anti-localization (WAL) [4] due to a large spin-orbit interaction. Much interest has also been paid to the enhanced thermoelectric efficiency in Bi nanowires [10-12], which is caused by increased electronic DOS near the Fermi level.

1.3.1 Bi band structure

The unique band structure of Bi with small effective mass leads to distinctive physical properties in low dimensional Bi. Bi has three highly non-parabolic electron pockets at *L*-point and one roughly parabolic hole pocket at *T*-point, as depicted in Figure 1.5 [37].

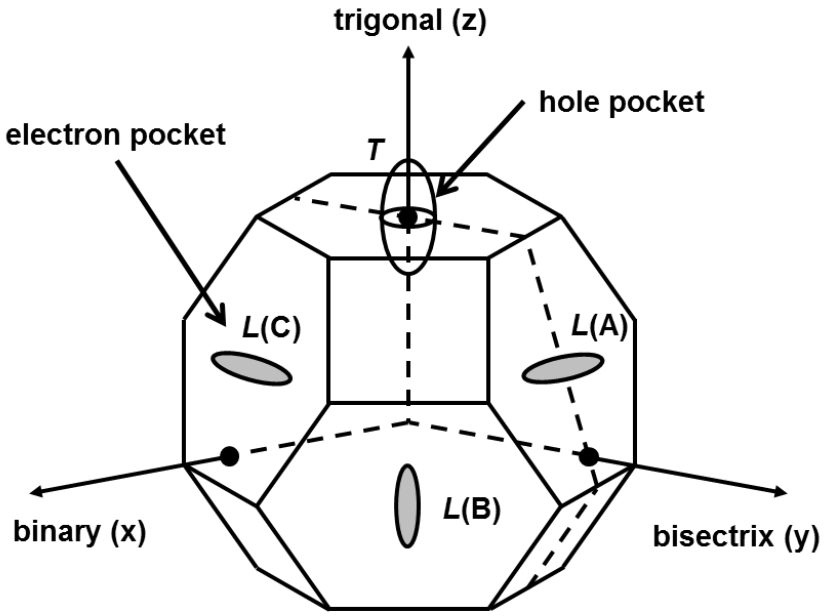

Figure 1.5 Fermi surfaces of Bi in Brillouin zone. There are three electron pockets at *L*-points and one hole pocket at *T*-point.

The effective mass values of non-parabolic bands near *L*-point are highly temperature dependent in comparison with those of parabolic band at *T*-point (Figure 1.6).This can be explained by effective mass tensors of Bi,

$$\mathrm{M}_{e,L} = \begin{pmatrix} m_{\mathrm{e1}} & 0 & 0 \\ 0 & m_{\mathrm{e2}} & m_{\mathrm{e4}} \\ 0 & m_{\mathrm{e4}} & m_{\mathrm{e3}} \end{pmatrix}$$

$$M_{h,T} = \begin{pmatrix} m_{\mathrm{e1}} & 0 & 0 \\ 0 & m_{\mathrm{e2}} & 0 \\ 0 & 0 & m_{\mathrm{e3}} \end{pmatrix}$$

The effective mass values of *L*-point conduction band at 0 K are m_{e1}=0.00118m_0, m_{e2}=0.263m_0, m_{e3}=0.00516m_0 and m_{e4}=0.0274m_0 where m_0 indicate the free electron mass [38]. The effective masses at the remaining two *L*-points can be calculate by rotating the original one by 120° and 240°. The effective mass elements of *T*-point valence band are m_{e1}=m_{e2}=0.059m_0, and m_{e3}=0.634m_0 [39]. Also, the *T*-point valence band locates around tetragonal axis, which is one of highly symmetry axes of the Brillouin zone. Thus, the effective mass is less temperature dependent. The effective mass at *L*-point as function of temperature can be described by [40],

$$\left(m_e(T)\right) = \frac{\left(m_0(T)\right)}{1 - 2.94 \times 10^{-3}T + 5.56 \times 10^{-7}T^2}$$

In addition, E_g is given by [40]

$$E_g = 13.6 + 2.1 \times 10^{-3}T + 2.5 \times 10^{-4}T^2(\text{meV})$$

The dispersion energy of*L*-point carriers is [41]

$$E_L(k) = -\frac{E_g}{2} \pm \frac{E_g}{2}\sqrt{1 + \frac{2\hbar^2}{E_g}\left(\frac{k_x^2}{m_x} + \frac{k_y^2}{m_y} + \frac{k_z^2}{m_z}\right)}$$

As a result, the band overlap (Δ_0) can have various values, depending of temperature: Δ_0 ~ -38 meV below 80 K and Δ_0 ~-104 meV at300 K [42].

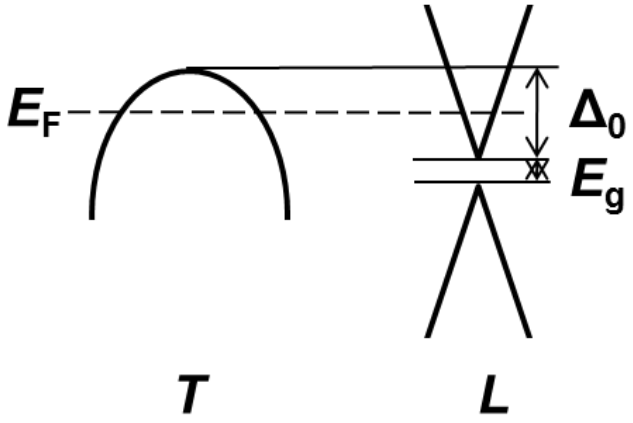

Figure 1.6 Bi band structures near the Fermi level. Δ_0 is band overlap between *L*-point conduction band and *T*-point valence band. E_g is small band gap at*L*-point.

Furthermore, the energy bands become discrete, as the dimensionality of Bi is lowered. In three dimensional Bi [37], DOS originating from the parabolic T-point valence band is presented to be

$$D(E) = \frac{1}{\mathrm{V}}\frac{dN}{dE} = \frac{\sqrt{2}}{\pi^2\hbar^3}(m_\mathrm{x}m_\mathrm{y}m_\mathrm{z})^{1/2}E^{1/2} \tag{1.6}$$

as usual DOS, $D(E) \propto E^{1/2}$.

In case of *L*-point, the energy dependence of wave vector *k* is given by,

$$k_i^E = \sqrt{\frac{2m_i}{\hbar^2}\left(\frac{E^2}{E_\mathrm{g}} - E\right)}$$

Additionally, a factor of 3 has to be considered ($3\times N(E)$) since there are three electron pockets at *L*-points. Finally, DOS is given by

$$D(E) = \frac{1}{\mathrm{V}}\frac{dN}{dE} = \frac{3\sqrt{2}}{\pi^2\hbar^3}\left(m_{\mathrm{x}}m_{\mathrm{y}}m_{\mathrm{z}}\right)^{\frac{1}{2}}\left(\frac{E^2}{E_{\mathrm{g}}} - E\right)^{\frac{1}{2}}\left(\frac{2E}{E_g} - 1\right) \tag{1.7}$$

The energy dependence of DOS behaves differently depending on the band shape, such as parabolic or non-parabolic. Therefore, in bulk, the DOS profiles of *L*-point conduction band and *T*-point valance band have very different shapes and temperature dependences, as shown in Figure 1.7 [37].

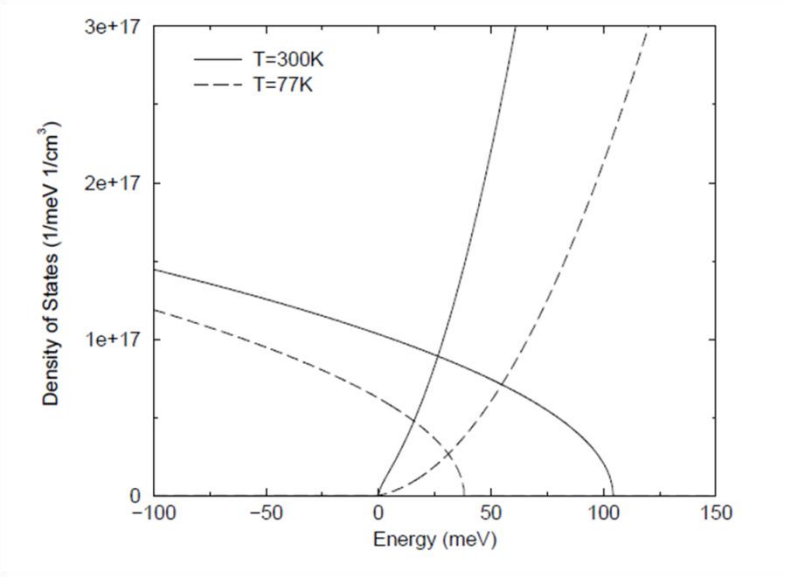

Figure 1.7 Bulk Bi densities of states of the *L*-point conduction band and *T*-point valance band at 77 K and 300 K. The zero of energy is taken as the bottom of the *L*-point conduction band [37].

In Bi nanostructures with sizes smaller than critical ones (diameter, thickness, etc.), a band gap opens up between the valence band at *T*-point and the conduction band at *L*-point below a critical temperature. To describe quantized energy states of confined electrons, Schrödinger' equation assuming so-called "square-well potential" with infinite potential wall can be used. For instance, energy state of Bi nanowire (one dimension) can be simply expressed as [37]

$$E(k_z) = \Delta_0 - \epsilon_{i,j} - \frac{\hbar^2 k_z^2}{2m_z}$$

where the long axis of nanowire is along the *z*-axis of Brillouin zone.

The subband energies of the non-parabolic *L*-point conduction band is given by

$$E_{i,j}^{L}(k_z = 0) = -\frac{E_g}{2} + \frac{E_g}{2}\sqrt{1 + \frac{4\epsilon_{i,j}}{E_g}}$$

where,

$$\epsilon_{i,j} = \frac{\pi^2\hbar^2}{2a^2}\left[\frac{i^2}{m_x} + \frac{j^2}{m_y}\right]$$

a is the diameter of nanowire and *i*, *j*=1,2,3…Figure 1.8.shows the calculated quantized energies of various bands in nanowire plotted as a function of diameter at 77 K. As can be seen, a gap opens below a critical diameter of 54.2 nm.

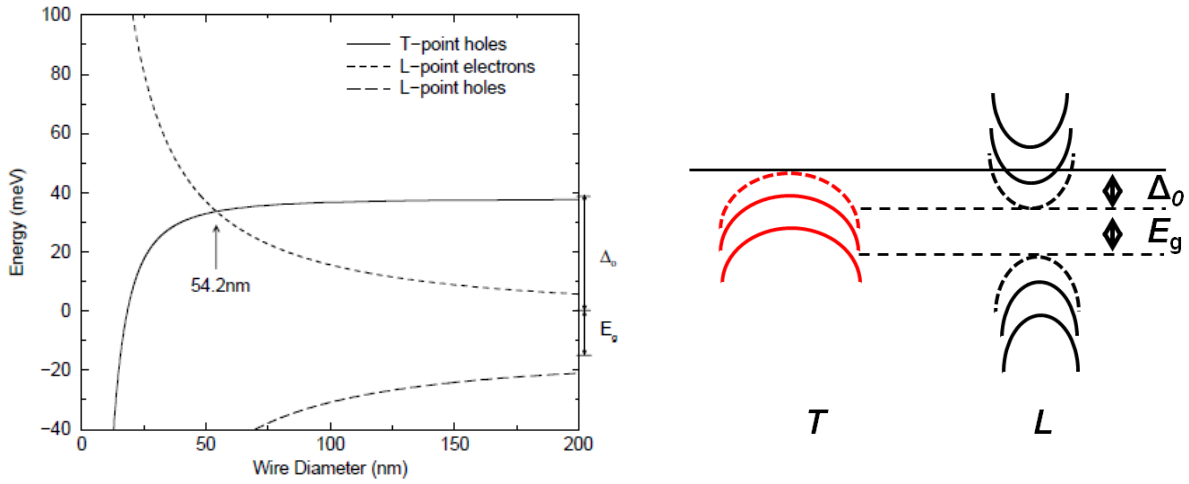

Figure 1.8.Calculatedsubband energies as a function of wire diameter at 77 K (left). Schematic illustration of the quantized band structures in low dimensional Bi (right) [37].

References

1. S. Lee, J. Ham. K. Jeon, J. Noh, and W. Lee, Nanotechnology **21**, 405701 (2010).
2. M. Rudolph and J. J. Heremans, Appl. Phys. Lett. **100**, 241601 (2012).
3. M. Rudolph and J. J. Heremans, Phys. Rev. B **83**, 205410 (2011).
4. N. Marcano, S. Sangiao, M. Plaza, L. Perez, A. F. Pacheco, R. Cordoba, M. C. Sanchez, L. Morellon, M. R. Ibarra, and J. M. De Teresa, Appl. Phys. Lett. **96**, 082110 (2010).
5. S. Sangiao, N. Marcano, J. Fan, L. Morellon, M. R. Ibarra, and J. M. De Teresa, EPL, **95**, 37002 (2011).
6. A. P. Alivisatos, Science **271**, 933 (1996).
7. S. Farhangfar, Phys. Rev. B **74**, 205318 (2006).
8. C. W. J. Beenakker and H. van Houten, Solid State Physics, **44**, 1 (1991).
9. Masaru Kuno, *Introductory Nanoscience*, page 203-235 (Garland Science, 2011).
10. J. P. Heremans, C. M. Thrush, D. T. Morelli, and M. C. Wu, Phys. Rev. Lett. **88**, 216801 (2002).
11. D. W. Song, W. N. Shen, B. Dunn, C. D. Moore, M. S. Goorshky, T. Radetic, R. Gronsky, and G. Chen, Appl. Phys. Lett. **84**, 1883 (2004).
12. A. Boukai, K. Xu, and J.R. Heath, Adv. Mater. **18**, 864 (2006).
13. C. A. Hoffman, J. R. Meyer, F. J. Bartoli, A. Di Venere, X. J. Yi, C. L. Hou, H. C. Wang, J. B. Ketterson, and G. K. Wong, Phys. Rev. B **48**, 11431 (1993).
14. S. Lee, J. Ham. K. Jeon, J. Noh, and W. Lee, Nanotechnology **21**, 405701 (2010).
15. S. Xiao, D. Wei, and X. Jin, Phys. Rev. Lett. **109**, 166805 (2012).

16. H. van Houten, B. J. van Wees and C. W. J. Beenakker, *Physics and Technology of Submicron Structures* (H. Heinrich, G. Bauer and F. Kuchar, eds.), Springer, Berlin, 1988.
17. E. Abrahams, P. W. Anderson, D. C. Licciardello and T. V. Ramakrishnan, Phys. Rev. Lett. **42**, 673 (1979).
18. P. W. Anderson, E. Abrahams, and T. V. Ramakrishnan, Phys. Rev. Lett. **43**, 718 (1979).
19. L. P. Gorkov, A. I. Larkin, and D. E. Khmel'nitskii, JETP Lett. **30**, 228 (1979).
20. G. Bergmann, Phys. Rep. **107**, 1 (1984); Phys. Rev. B **28**, 2914 (1983).
21. A. I. Larkin and D. E. Khmel'nitskii, Sov. Phys. Usp. **25**, 185 (1982).
22. D. E. Khmel'nitskii, Physica B **126**, 235 (1984).
23. R. P. Feynman and A. R. Hibbs, *Quantum Mechanics and Path Integrals*, (McGraw-Hill, New York, 1965).
24. V. F. Gantmakher, *Electrons and Disorder in Solids* (Oxford Science Publications, 2005).
25. B. L. Altshuler, A. G. Aronov and D. E. Khmelnitskii, J. Phys. C **15**, 7367 (1982).
26. S. Hikami, A. I. Larkin and Y. Nagaoka, Prog. Theor. Phys. **63**, 707 (1980).
27. P. H. Woerlee, G. C. Verkade and A. G. M. Jansen, J. Phys. C: Solid State Phys. **16**, 3011 (1983).
28. C. Kurdak, Phys. Rev. B 46, 6846 (1992).
29. B. L. Altshuler, A. G. Aronov and P. A. Lee, Phys. Rev. Lett. **44**, 1288 (1980).
30. D. Schiferl and C. S. Barrett, J. Appl. Crystallogr. **2**, 30 (1969).

31. J. Heremans, C. M. Thrush, Y. M. Lin, S. Cronin, Z. Zhang, M. S. Dresselhaus, and J. F. Mansfield, Phys. Rev. B **61**, 2921 (2000).
32. G. E. Smith, J. M. Rowell, and G. A. Baraff, Phys. Rev. A **135**, 1118 (1964).
33. V. S. Edel'man, Adv. Phys. **25**, 555 (1976).
34. N. Garcia, Y. H. Kao, and M. Strongin, Phys. Rev. B **5**, 2029 (1972).
35. H. Asahi, T. Humoto, and A. Kawazu, Phys. Rev. B **9**, 3347 (1974).
36. F. Y. Yang, K. Liu, K. Hong, D. H. Reich, P. C. Searson, and C. L. Chien, Science, **284**, 1335 (1999).
37. Stephen B. Cronin, *Electronic Properties of Bi Nanowires*, Ph.D. thesis, Massachusetts Institute of Technology (2002).
38. J. Heremans and O. P. Hansen, J. Phys. C **12**, 3483 (1979).
39. R. T. Isaacson and G. A. Williams, Phs. Rev. **185**, 682 (1969).
40. M. P. Vecchi and M. S. Dresselhaus, Phys. Rev. B **10**, 771 (1974).
41. B. Lax and J. G. Mavroides, *Solid state Physics*, page 261 (Academic Press, New York, 1960).
42. C. F. Gallo, B. S. Chandrasekhar and P. H. Sutter, J. Appl. Phys. **34**, 144 (1963).

Chapter 2

Experimental Methods

This chapter introduces the outlines of the techniques used for sample fabrication and characterization. I fabricated Bi anti-dot samples base on PVD (physical vapor deposition) method in a self-assembled manner on AAO template. Transport and magneto-transport properties were measured by conventional four or six probe method.

2.1 Anodized Aluminum Oxide (AAO) template

The template technique is useful for tuning the dimensions of nanostructures, such as diameters and thicknesses of nanowire [1], nanodot [2] and nanoring [3]. Among various templates, anodized aluminum oxide (AAO) membrane is one of the well-known and well-established ones. Figure 2.1 shows AAO membranes which consist of a highly ordered pore array with nano-scale diameter and high aspect ratio in a large area.

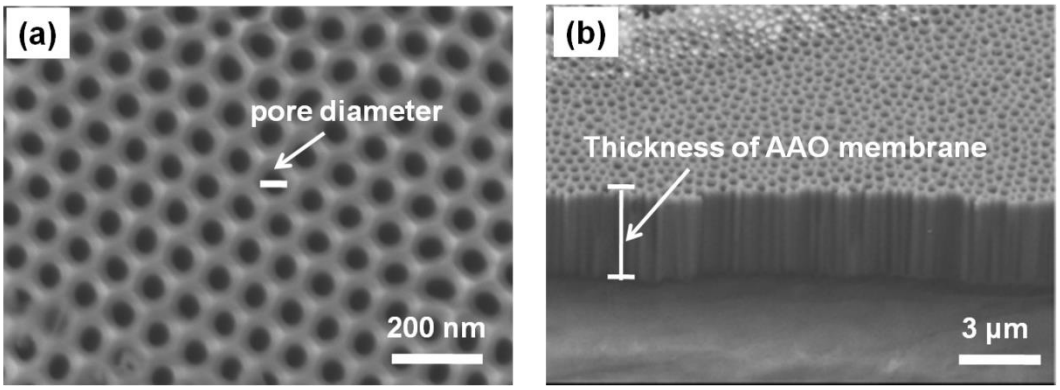

Figure 2.1.(a) top-view and (b) cross-sectional SEM images of an AAO membrane with a mean pore diameter of 45.2 nm and a thickness of 3.2 μm.

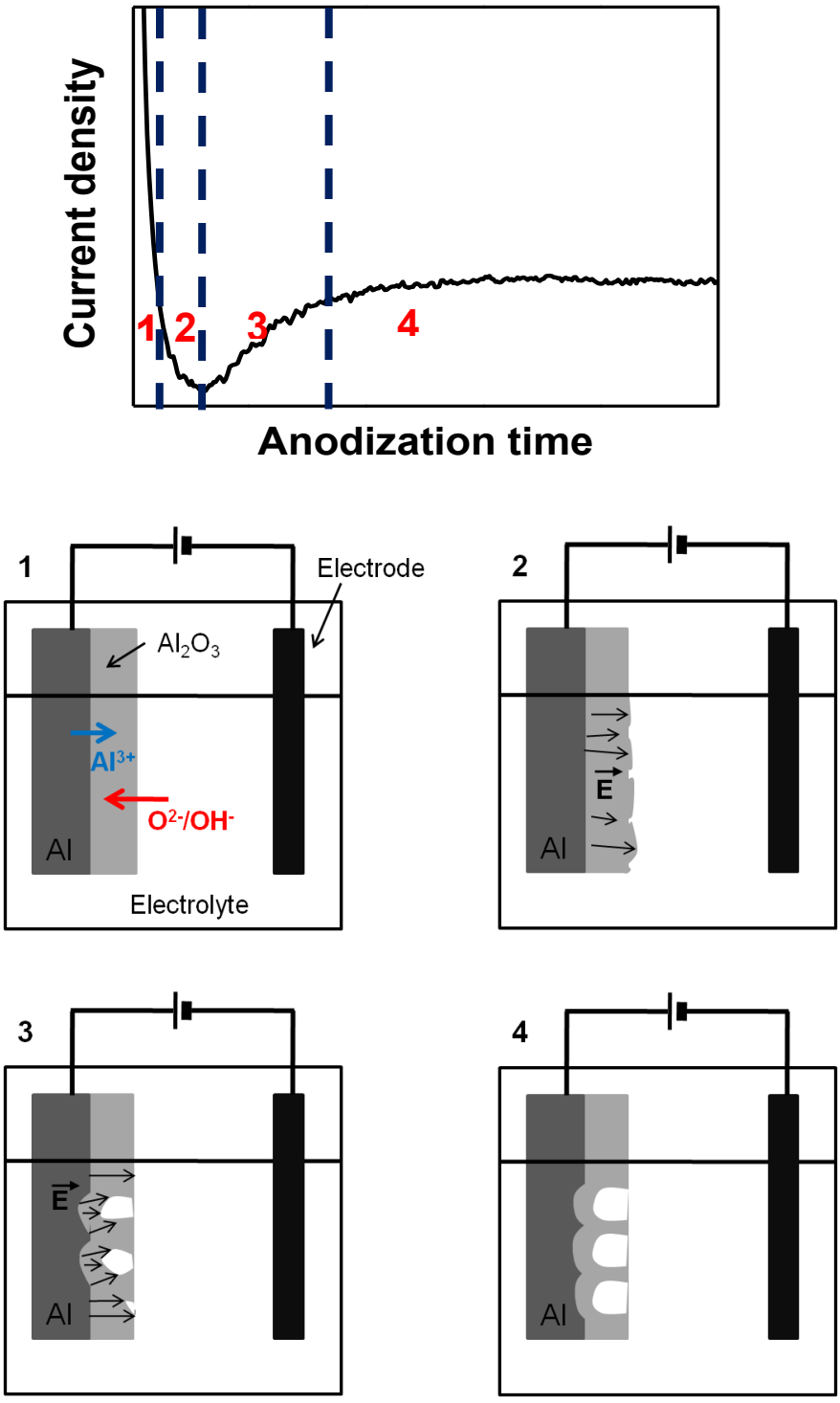

Figure 2.2.Schematics of initial pore formation mechanisms during anodization.

The pore formation mechanism by anodization processes can be classified into four stages, as seen from a typical current density vs time curve during anodization in Figure 2.2 [4-8]. In the first stage of anodization, current density significantly decreases due to the formation of a thin alumina layer on the entire Al surface. In the second stage, the current density reaches the minimum value because electric field is focused on local regions, which leads to surface fluctuations. In the third stage, the oxidized reaction proceeds faster in the regions where the electric field is concentrated and pore structures were constructed there. In the final stage where the current density is stable, the pores grow in the vertically direction.

In this study, to obtain regularly arranged straight pores, two-step anodization processes [9] are performed, as shown in Figure 2.3. An Al foil was first electropolished in a mixture of ethanol and perchloric acid to remove a natural oxide layer and to make the surface smooth. After the chemical polishing process, the surface of the Al foil becomes mirror-like. Then, the two-step anodization processes are conducted in a low-temperature electrolyte under a constant voltage. There are three famous electrolytes for Al anodization: sulfuric acid, oxalic acid and phosphoric acid and the pore diameters vary depending on the electrolyte [10]. Each electrolyte requires different anodization time and electrolyte concentration as well as applied voltage. Therefore, the pore diameters can be dramatically varied by changing the anodization conditions. Figure 2.4 (a) is a SEM image of AAO prepared by anodization in 0.3 M oxalic acid under a constant voltage of 40 V at 5 °C. In this case, the mean pore diameter is 45 nm. Whereas, the porous structure obtained in 10 *wt*% phosphoric acid under 150 V at 4 °C has a mean pore diameter of 200 nm (Figure 2.4 (b)).

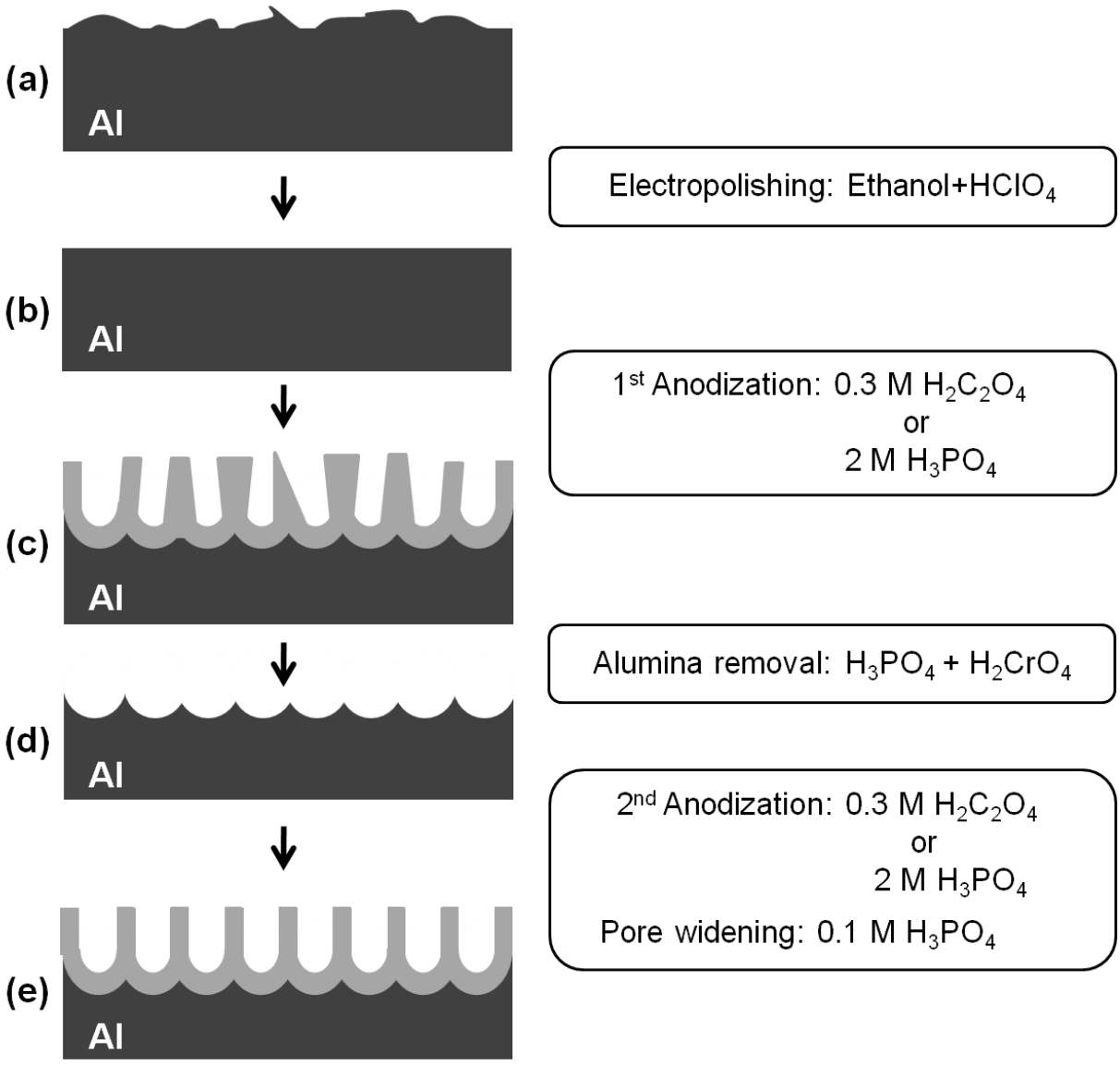

Figure 2.3 Schematics for the formation of porous alumina membrane by anodization processes.

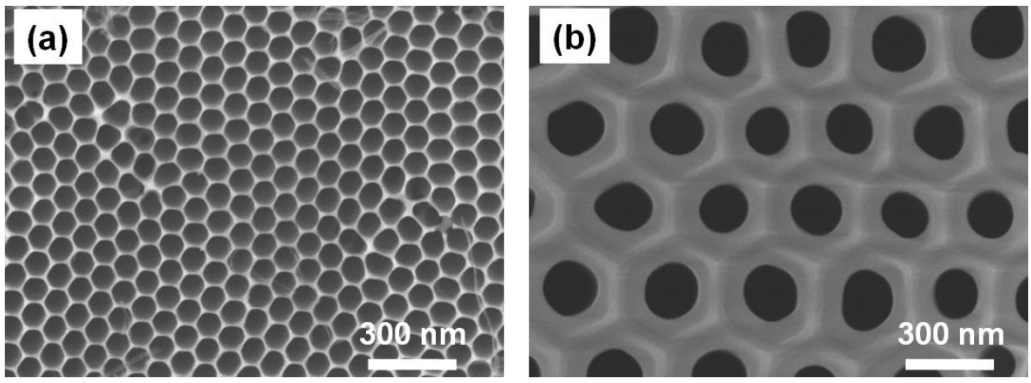

Figure 2.4 Top-view SEM images of AAO membrane obtained with (a) oxalic acid and (b) phosphoric acid. The mean pore diameters are 45 nm and 200 nm, respectively.

Before the 2nd anodization, the randomly grown porous alumina structure was dissolved by using a mixture of phosphoric acid and chromic acid at 60°C. Therefore, regularly arranged imprint pore structures were left on the Al surface, which allows the formation of ordered porous alumina layer during the 2nd anodization process in Figure 2.3 (d). This alumina layer was dipped into phosphoric acid for pore widening, which enabled to tailor the length of pore wall width and the thickness of alumina layer. Figure 2.5 shows SEM images of AAO in which the thicknesses of alumina layer and pore walls were tuned by pore widening time: In Figure 2.5 (a) and Figure 2.5 (b), the pore widening was conducted for 1 h and 2 h for, respectively.

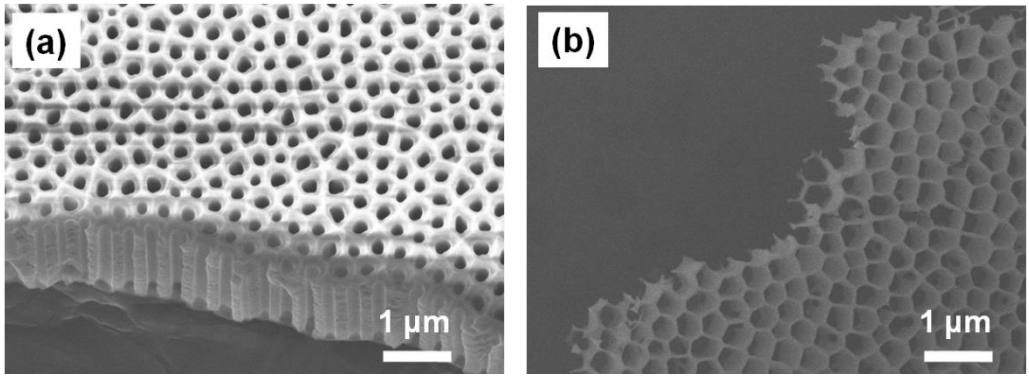

Figure 2.5 Cross-sectional SEM images of AAO membranes anodized by 10 *wt%* phosphoric acid. The pore widening process after 2nd anodization was carried out for (a) 1 h and (b) 2 h.

2.2 Thin Film deposition

2.2.1 Radio frequency sputtering (RF-sputtering)

In this study, Al thin films were used to fabricate porous alumina template. For stable anodization, smooth and uniform surface in large area as well as denser films with smaller grain of Al thin films are needed. In addition, good adhesion between substrate and Al thin films is necessary. Therefore, I used RF-sputtering as shown in Figure 2.6. The RF-sputtering system enabled to precisely control the growth of Al thin films by changing the pressure of Ar gas, distance between Al target and substrate and sputtering power.

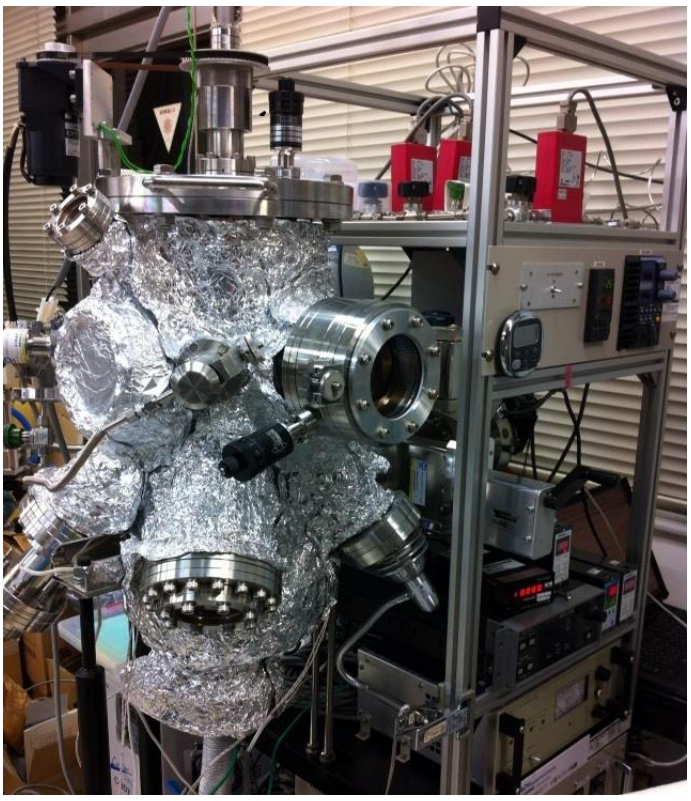

Figure 2.6.A photo of sputtering machine (AOV SPAR-211).

2.2.2 Thermal evaporation

To investigate the relation between transport properties and dimensionality in Bi anti-dot thin films, the thickness of Bi film must be precisely controlled. Furthermore, the porous surface structures of AAO have to be maintained during the deposition of Bi anti-dot films. Thermal evaporation is a very good candidate for this purpose, because the deposition rate and film thickness can be monitored in real time by a quartz sensor inside the vacuum chamber.

The thickness of the deposited film is estimated from a change in resonance frequency of the quartz sensor, which increases along with the weight gain of the sensor as a consequence of film deposition [11]. Additionally, in-situ thickness measurement is the best way for accurate measurement of physical properties, because Bi thin films are easily scratched by the probe tip of mechanical thickness measurement system. Such In-situ monitoring can also minimize the exposure time of Bi in air and thus the formation of oxidized layer.

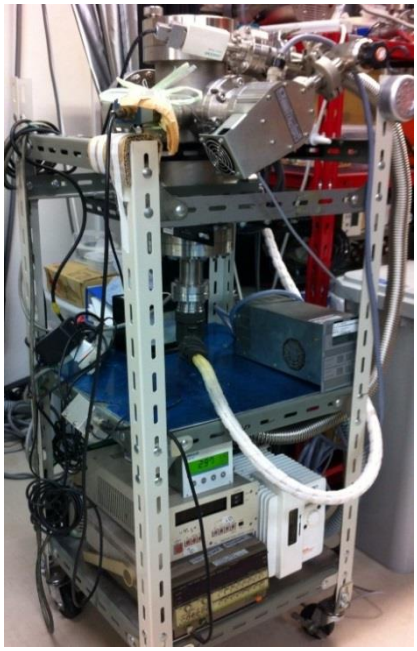

Figure 2.7.Laboratory-constructed thermal evaporation system.

2.3 Electrical transport measurements

Electrical resistivity and carrier concentration evaluated by Hall Effect are fundamental transport properties. I measured electrical resistance by conventional four probe method and Hall voltage by six probe method with physical property measurement system (PPMS, Quantum Design). Two probes in Figure 2.8 are served as current electrodes and the other four probes are for longitudinal and transverse voltages measurements. Magnetoresistance (MR) measurements were also performed under external magnetic field perpendicular to the sample surfaces. In this study, transport and magneto-transport measurements were conducted in a temperature range from 2 K to room temperature. Magnetic field was first swept form 0 T to ±9 T and then returned to 0 T.

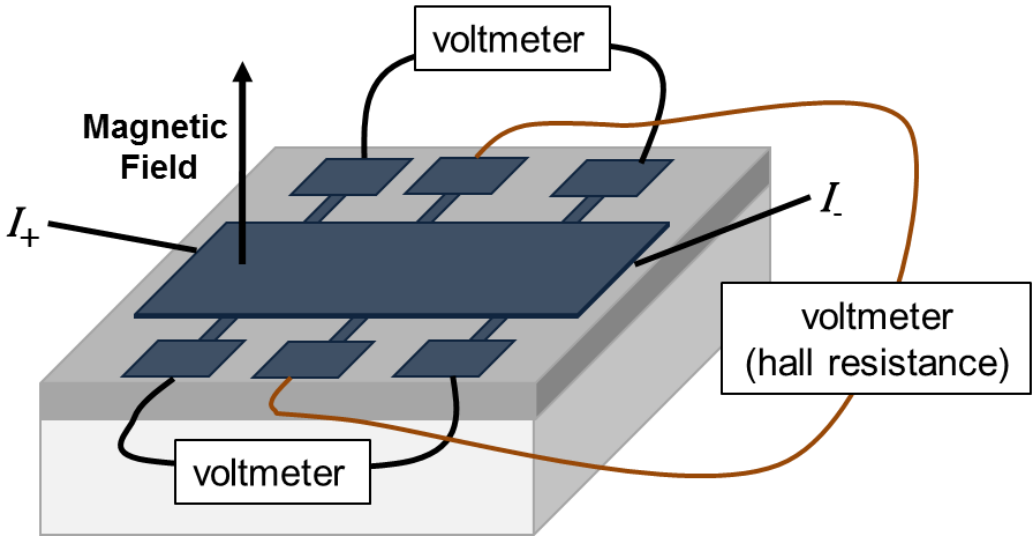

Figure 2.8.Schematics for six probe measurement.

References

1. D. Xu, D. Chen, Y. Xu, X. Shi, G. Guo, L. Gui and Y. Tang, Pure Appl. Chem. **72**, 127 (2000).

2. X. Gao, L. Liu, B. Birajdar, M. Ziese, W. Lee, M. Alexe and D. Hesse, Adv. Funct. Mater. **19**, 3450 (2009).

3. S. Zhao, H. Roberge, A. Yelon and T. Veres, J. Am. Chem. Soc. **128**, 12352 (2006).

4. J. W. Diggle, T. C. Downie and C. W. Coulding, Chem. Rev. **49**, 365 (1969).

5. F. Li, L. Zhang and R. M. Metzger, Chem. Mater. **10**, 2470 (1998).

6. R. B. Wehrspohn, A. P. Li, K. Nielsch, F. Muller, W. Erfurth and U. Gösele, "Highly ordered alumina films: pore growth and applications" (Oxide Films in The Electrochemical Society Proceeding Series), vol. PV 2000-4, pp271. Pennington, NJ: Marcel Dekker (2000).

7. Jinsub Choi, *Fabrication of monodomain porous alumina using nanoimprint lithography and its applications*, Ph.D. thesis, Mathematisch-Naturwissenschanftlich-TechnischemFakultät der Martin-Luther-Universität Halle-Wittenberg (2003).

8. A. M. Abd-Elnaiem and A. Gaber, Int. J. Electrochem. Sci. **8**, 9741 (2013).

9. H. Masuda and K. Fukuda, Science, **268**, 1466 (1995).

10. A. P. Li, F. Müller, A. Birner, K. Nielsch, and U. Gösele, J. Appl. Phys. **84**, 6023 (1998).

11. V. M. Mecea, Sensors and Actuators A,**128**, 270 (2006).

Chapter 3

Fabrication of Bi anti-dot thin films

In this chapter, I discuss the effect of surface roughness of Al thin films on the anodization process. Fabrication method of Bi anti-dot thin films with tuned pore wall widths is also presented.

3.1 Preparation of porous alumina template

In order to fabricate anodized aluminum oxide (AAO) templates with highly ordered pore arrays, it is much better to use bulk Al foils (~mm) than Al thin films deposited on substrates. This is because Al thin films are generally composed of smaller grains than Al bulk foils, which leads to random pore growth [1]. In addition, long time 1^{st} anodization process, which gives "foot prints" for 2^{nd} anodization to form highly ordered pore structures [2, 3], cannot be conducted for Al thin films. However, for investigating the physical properties of fabricated nanostructures on AAO templates, the porous alumina layer should be highly insulating. The porous alumina templates made of bulk Al foils contain residual Al, and thus an additional removal process is needed. During this process, the thin alumina layer ranging from ~μm to ~nm is easily broken. Furthermore, thin alumina layer has difficulty in handling, as well. To avoid these problems, used Al thin films for anodization, which enables not only direct deposition of

metal films on AAO template but also easy handing of the alumina layer that is attached on solid substrate after anodization.

3.1.1 Physical vapor deposition of aluminum thin films

Aluminium (Al) thin films with thicknesses of ~500 nm were deposited on unheated α-Al_2O_3 (0001) substrate by RF-magnetron sputtering, where a high purity Al target (99.999 %) was used. To investigate the effect of surfaces roughness on the growth of alumina layer, two different deposition conditions are examined: one is continuous deposition and the other is cyclic deposition [4], in which deposition of 90 nm-thick layer and 30 minutes cooling were alternatively repeated. In the latter method, it is possible to suppress the coalescence of grains during the deposition because the substrate temperature is kept lower. The base pressure was maintained at 5 x 10^{-5} Pa and the working pressure was set to 3.25 x 10^{-1} Pa under Ar gas flow of5 standard cubic cm per minute (sccm) at room temperature. The deposition power and its density were 250 W and 12.3 Wcm^{-2}, respectively. The surface roughness was evaluated by field emission scanning electron microscope (FE-SEM) and atomic force microscope.

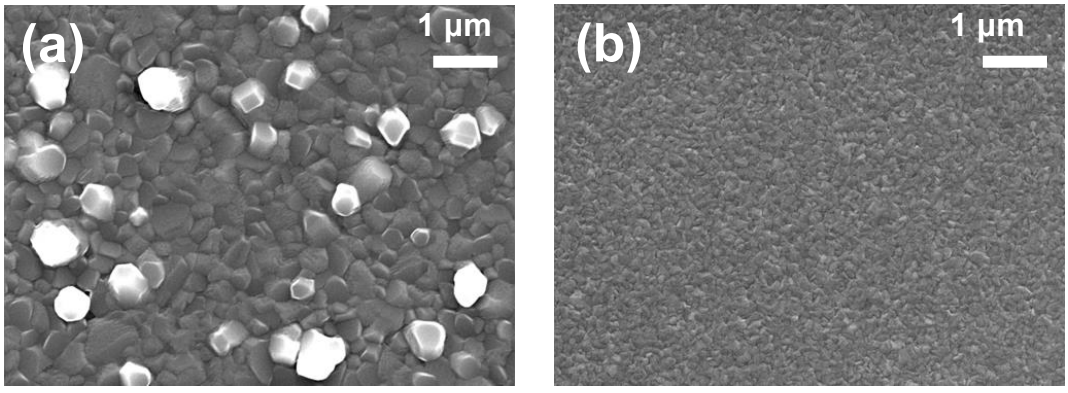

Figure 3.1.SEM images of Al thin films on sapphire substrate. (a) continuous deposition and (b) cyclic deposition.

Figure 3.1 show SEM images of 500 nm-thick Al thin films deposited with the two different deposition methods. The difference in the deposition methods led to different adatoms diffusion on substrate. As is well known, grain coalescence by grain boundary migration is affected by the surface diffusion rate [5]. In case of the cyclic deposition, thermal energy is taken away during the cooling period after adatoms reach room temperature substrate. Therefore the thermodynamic driving force of adatoms in the cyclic deposition is lower than that in continuous deposition. In other words, the surface diffusion rate is slower in the cyclic deposition. At the first stage of deposition, adatoms settle down on the substrate surface, after almost covering the substrate and grains are merged with neighboring ones [6, 7, 8]. Thus, in the cyclic deposition, grain coalescence is suppressed, which leads to larger film density with very small size grains, as seen from Figure 3.2. Indeed, the root mean square (RMS) values of the surface roughness were estimated to be 18.6 nm for continuous deposition and 7.7 nm for cycle deposition.

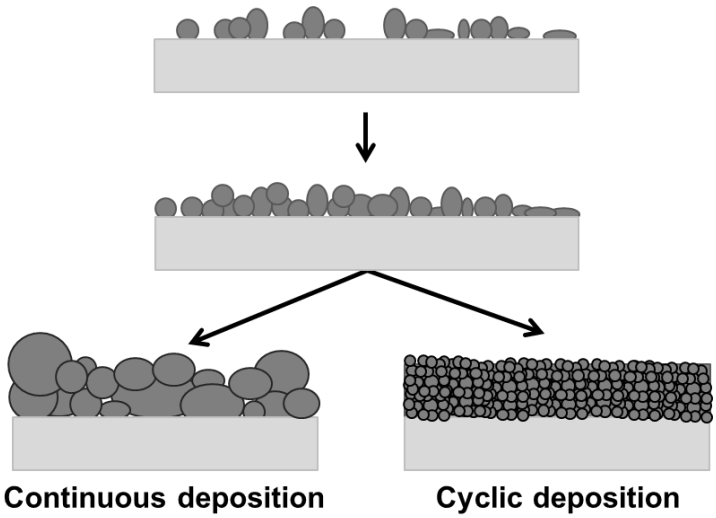

Figure 3.2.Schematics of grain growth and coalescence during film deposition.

3.1.2 Influence of anodization process on the surface of Al thin films

The Al thin films deposited on sapphire substrates were subjected to two times anodization process [2] with 0.3 M oxalic acid solution under the constant voltage of 40 V at 4 °C for 12 min. After the1stanodization, an initially formed alumina layer with an irregular pore array was removed by using a mixture of phosphoric acid and chromic acid at 60 °C for 30min. Therefore, the films after the 1st anodization were served only as "foot-prints" for 2nd anodization explained in Figure 2.3. The 2nd anodization ran in the same condition with the 1st one until current becomes zero, which means that the aluminum thin film was completely changed to alumina. Subsequently, the pore widening process was performed by dipping the film into phosphoric acid at 30 °C to remove residual Al and control pore wall width. Since the anodization processes were carried out anodization immediately after taking the Al films out of the vacuum chamber in this experiment, I did not perform further electro-polishing, which is usually conducted for peeling off a surface alumina layer naturally formed in air.

It should be noted that the surface roughness of the film after 1st anodization was greatly influenced by the surface structure of Al thin films before anodization. Figure 3.3 compares top-view SEM images of the films after 1st anodization prepared from the Al thin films deposited by continuous deposition and cyclic deposition. As seen from Figure 3.3 (a), the former film exhibits a rough surface with large grains, whereas the latter film is much flatter (Figure 3.3 (b)). This implies that the morphology of initial Al film, including roughness and grain size, was transferred to that of anodized one.

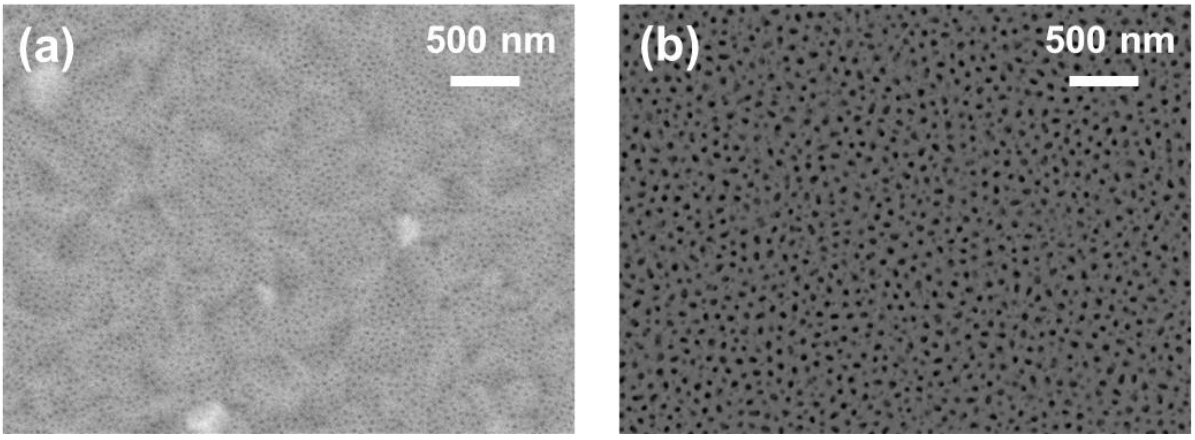

Figure 3. 3. Top view of alumina layer after 1st anodization of Al thin films deposited by (a) continuous deposition and (b) cyclic deposition.

Figure 3.4 shows surface SEM images after 2nd anodization together with current density (*I*) vs time (*t*) curves during the 2nd anodization. Detailed current density behavior during anodization was explained in Chapter 2. In case of the film prepared from the continuously deposited Al film (Figure 3.3 (a)),a two-stage feature is visible in the *I-t* curve (Figure 3.4 (a)). The rapidly decreasing current density at $t<10$ s corresponds to the initial pore formation on foot prints made by the 1stanodization. After 10 s, in contrast, the current density dropped to almost zero, which means that the Al film is completely changed to alumina. However, there was no stable ordered pore array and, thus, the total anodization time was very short. From the *I-t* curve, unstable anodized reactions, such as local burning, were thought to occur, which is consistent with the corresponding SEM image (Figure 3.4 (b) with an irregular pore array as well as a very thin alumina layer remaining on substrate. The inset in Figure 3.4 (b) confirms a rough surface even after the 2nd anodization. Whereas, the *I-t* curve of the film prepared from cyclic deposition

shows very distinctive behavior during the 2nd anodization. That is, the current density increased at 50 s <*t*< 200 s and then became almost constant at *t* > 200 s, being a signature of stable anodizing as seen in usual anodization processes [9, 10]. I used the latter film as an AAO template for further experiments, because a smoother template is suitable for attaining high adhesion on sapphire substrate.

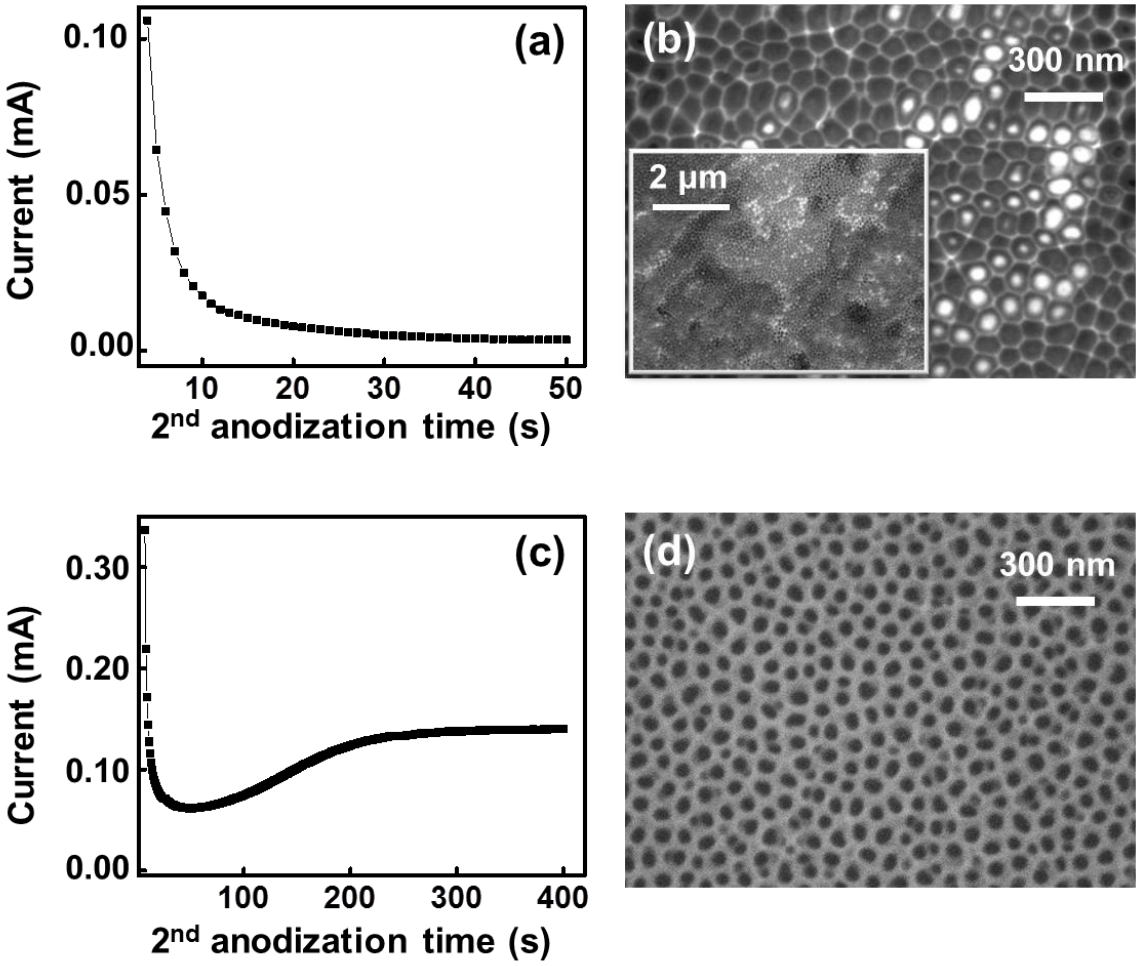

Figure 3.4.Current density vs time curves during 2nd anodization under constant applied voltage measured for the Al thin films fabricated by (a) continuous and (c) cyclic deposition. (b) and (d) are corresponding top-view SEM images after 2nd anodization.

The two different anodization reactions described above can be rationalized by the considering surface roughness and grains size of the Al thin films. In conventional AAO made of Al foil, oxide hillocks on the surfaces of Al foils play an important role in stable anodization because undulating surfaces results in current concentration on top of the protruding oxide hillocks which arise from rapid oxide growth along with mechanical stresses around the hillock areas, as illustrated in Figure 3.5. Consequently, a crack is generated in the vicinity of the hillocks, which enhances local burning during anodization [11-13]. In terms of the surface roughness, the cyclic deposition restricts the growth of Al thin films with undulating surface and large grains. In addition, a smoother surface with small grains prevents local burning during anodization. In the AAO template prepared from Al thin film, I can control not only the oxide growth rate by preventing local current concentration but also the local mechanical stress during oxide growing, although the regularity of the pore ordering is not so high compared with that of conventional AAO by Al foil.

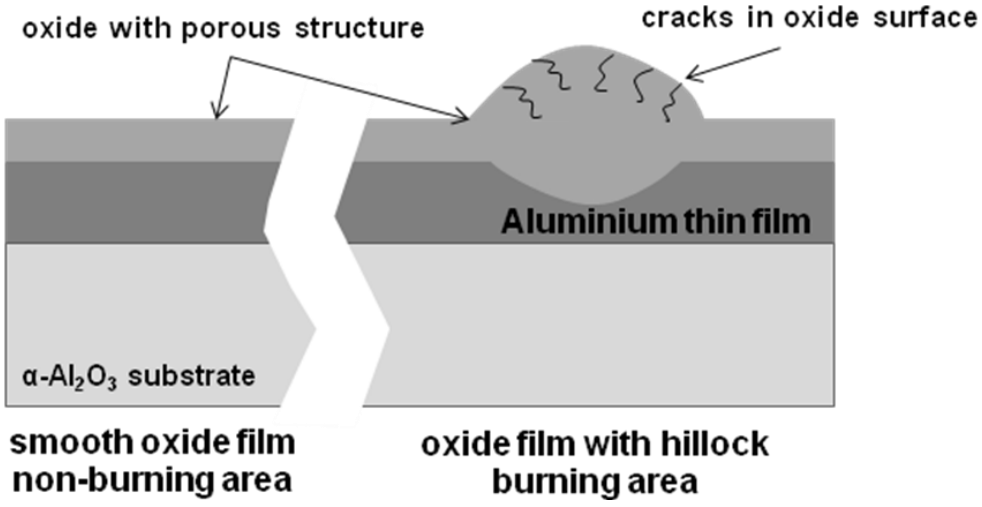

Figure 3.5. Schematic illustrate of the two different surface structures.

3.1.3 Modulated porous structure

To tailor pore wall width (w_{AAO}) in more flexible manner, the alumina layer has to be enough thick to stand the pore widening process after 2nd anodization. The surface structure is almost unchanged, when the thickness of the Al thin film exceeds 500 nm Al. Therefore, 0.8-1 μm-thick Al was deposited on sapphire substrate by cyclic method under the same condition as that of the 500 nm-thick Al thin films. By changing the pore widening time using a phosphoric acid solution, w_{AAO} was varied in a range of 30-60 nm. Figure 3.6 shows plain-view SEM images of the anodized aluminum oxide (AAO) films thus prepared with w_{AAO} of 30 nm (Figure 3.6. (a)) and of 60 nm (Figure 3.5. (b)), indicating good controllability of the pore wall width. Note that w_{AAO} =30 nm is shorter than λ_F (~ 40 nm), while w_{AAO} =60 nm is longer.

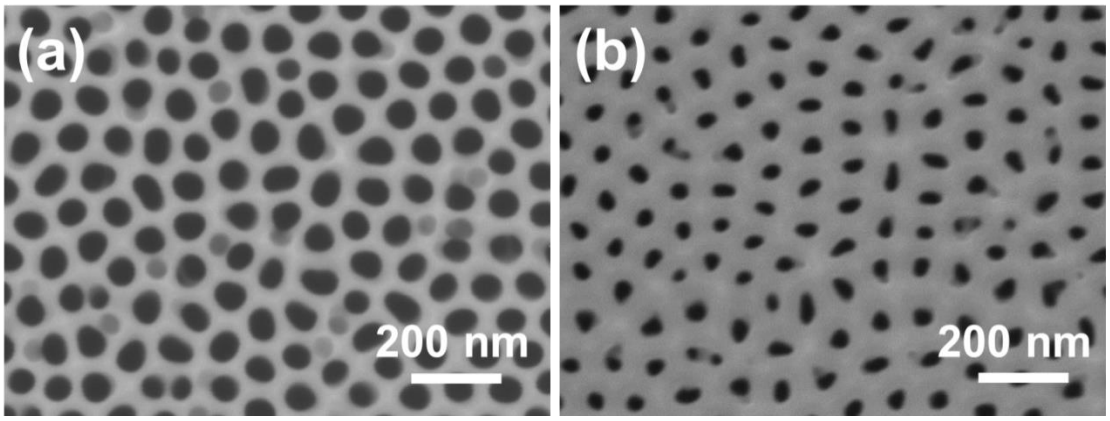

Figure 3. 6.SEM images of AAO templates with tailored pore wall widths (w_{AAO}). (a) w_{AAO}=30 nm and (b)w_{AAO}=60 nm.

3.2 Thermal deposited Bi anti-dot thin films

On the AAO templates, Bi films with three different thicknesses (t) of 25 nm, 35 nm and 50 nm were deposited by thermal evaporation at 10^{-5} Pa with a deposition rate of 0.17 nm/s at room temperature.

Figures 3.7 (a),(b) and (c) show SEM images of the 25 nm-thick, 35nm-thick and 50nm-thick Bi films deposited on AAO templates with w_{AAO}=30 nm. A SEM image in Figure 3.7 (d) indicates 25 nm-thick Bi anti-dot structure formed on the AAO temperate with w_{AAO}=60 nm. These figures clearly demonstrate the formation of Bi anit-dot structures on the AAO templates. As seen from Figure 3.7, the actual pore wall widths (w_{Bi}) of the thicker films are wider than w_{AAO}=30 nm due to the lateral growth of the Bi films, as schematically illustrated in Figure 3.8, while the 25 nm-thick film has almost the same wall width as w_{AAO}=30 nm. The averaged w_{Bi} values evaluated from the SEM images are 38 nm, 48 nm and 57 nm for the 25 nn-thick, 35 nm-thick and 50 nm-thick Bi films, respectively, with w_{AAO}=30 nm, as seen from the histograms in Figure 3.7. On the AAO template of w_{AAO}=60 nm, however, only 25 nm-thick Bi films showed the anti-dot structure with w_{Bi}=76 nm. Figure 3.9 shows a SEM image of the 50 nm-thick Bi films on w_{AAO}=60 nm, from which the anti-dot structure is hardly recognizable.

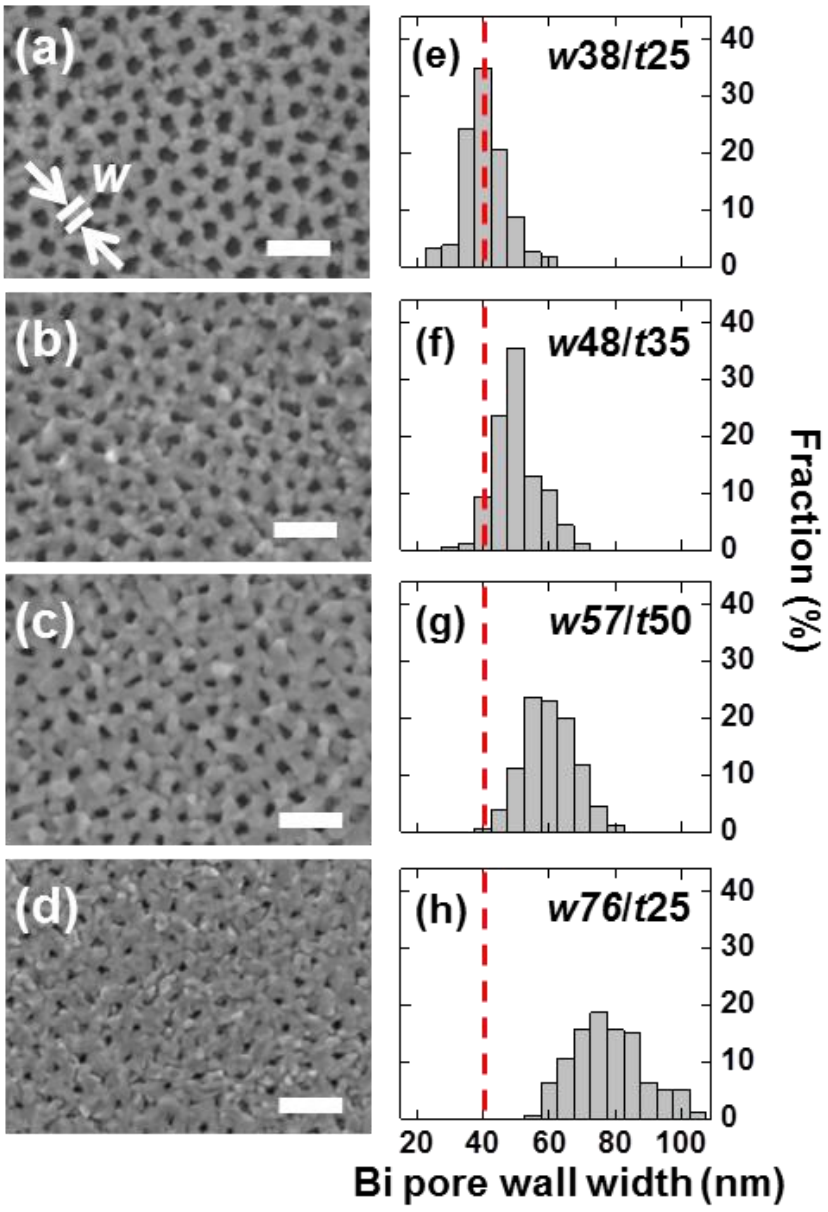

Figure 3.7.(a−d) Plain-view SEM images of Bi anti-dot films on AAO templates with (a−c) w_{AAO} = 30 nm or (d) w_{AAO} = 60 nm (d); (a, d) t = 25 nm, (b) t = 35 nm and (c) t = 50 nm. Scale bars represent 200 nm in all images. (e−h) Histograms for distribution of pore wall widths evaluated from Fig. 3.7(a−d), respectively.

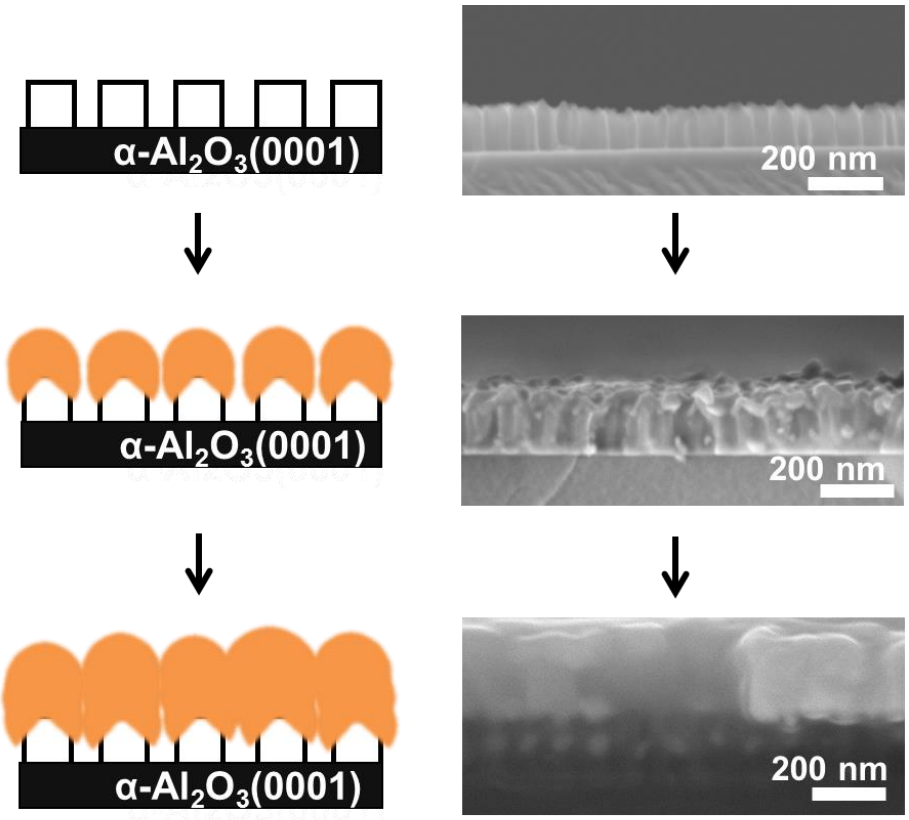

Figure 3.8.Formation of anti-dot structures on AAO template.

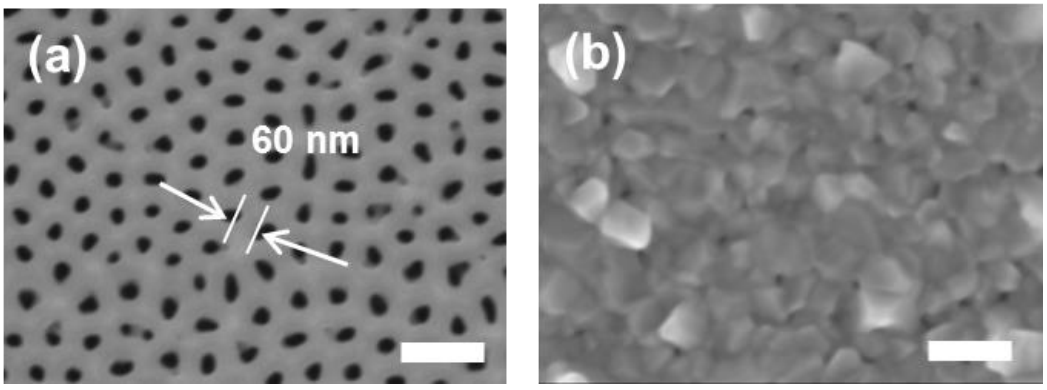

Figure 3.9. SEM images of (a)AAO template with 60 nm pore wall widths and (b)50 nm-thick Bi thin films deposited on (a).

References

1. Z. Sun and H. K. Kim, Appl. Phys. Lett. **81**, 3458 (2002).

2. H. Masuda and K. Fukuda, Science, **268**, 1466 (1995).

3. T. S. Kustandi, W.w.Loh, H. Gao and H. Y. Low, ACS Nano. **4**, 2561 (2010).

4. S. Z. Chu, K. Wada, S. Inoue and S. Todoroki, J. Electrochem. Soc. **149**, B321 (2002).

5. J. A. Thornton, Annu. Rev. Mater. Sci. **7**, 239 (1977).

6. C. V. Thornton, Annu. Rev. Mater. Sci. **30**, 159 (2000).

7. G. H. Gilmer, H. Huang, T. D. Rubia, J. D. Torre and F. Baumann, Thin Solid Films **365**, 189 (2000).

8. I. Petrov, P. B. Barna, L. Hultman and J. E. Greene, J. Vac. Sci. Technol. A **21**, S117 (2003).

9. F. Li, L. Zhang and R. M. Metzger, Chem. Mater. **10**, 2470 (1998).

10. A. M. Abd-Elnaiem and A. Gaber, Int. J. Electrochem. Sci. **8**, 9741 (2013).

11. D. J. Arrowsmith, P. J. Cunningham, Trans. Inst. Met. Finish. **60**, 5 (1982).

12. S. Ono, M. Saito, M. Ishiguro, H. Asoh, J. Electrochem. Soc. **151**, B473 (2004).

13. T. Aerts, I. E. Graeve, H. Terryn, ElectrochimicaActa, **54**, 270 (2008).

Chapter 4

Low dimensional properties of Bi anti-dot thin films

The quantum confinement effects (QCE) in Bi anti-dot thin films grown on anodized aluminium oxide templates were investigated. The pore wall widths (w_{Bi}) and thickness (t) of the films were tailored to have values longer or shorter than Fermi wavelength of Bi (λ_F =~40 nm) in order to control the dimensionality. Firstly, magnetic field dependent resistance was measured at several temperature regimes. The result revealed a well-defined weak anti-localization (WAL) effect below 10 K. After that, coherence lengths (L_ϕ) as functions of temperature were derived from the magnetoresistance vs field curves by assuming the Hikami-Larkin-Nagaoka model [1]. The influence of w_{Bi} and t on low dimensionality of Bi anti-dot thin films was discussed by power-law fitting. Therefore, I figure out that w_{Bi} and t with smaller than λ_F showed low dimensional electronic behavior at low temperatures where $L_\phi(T)$ exceed w_{Bi} or t.

This chapter published in Applied Physics Letters

"Y. Park, Y. Hirose, S. Nakao, T. Fukumura, J. Xu and T. Hasegawa, Appl. Phys. Lett.104, 023106 (2014)"

4.1 Weak anti-localization effects in Bi anti-dot thin films

For Bi anti-dot thin films with tuned pore wall widths and films thicknesses, magnetoresistance (MR) measurements were performed from room temperature to 2 K in conventional four-probe geometry. The external magnetic field (H) was applied perpendicular to the film surfaces. Figure 4.1displays MR (%) = $100\times[R(H,T)-R(0,T)]/R(0,T)$ vs H curves obtained for the Bi anti-dot films with w_{Bi} = 38 nm (w_{AAO} = 30 nm) and t = 25 nm, hereafter denoted as (w38/t25), at various temperatures. As seen from the Figure 4.1, the MR-H curves drastically changed with respect to temperature.

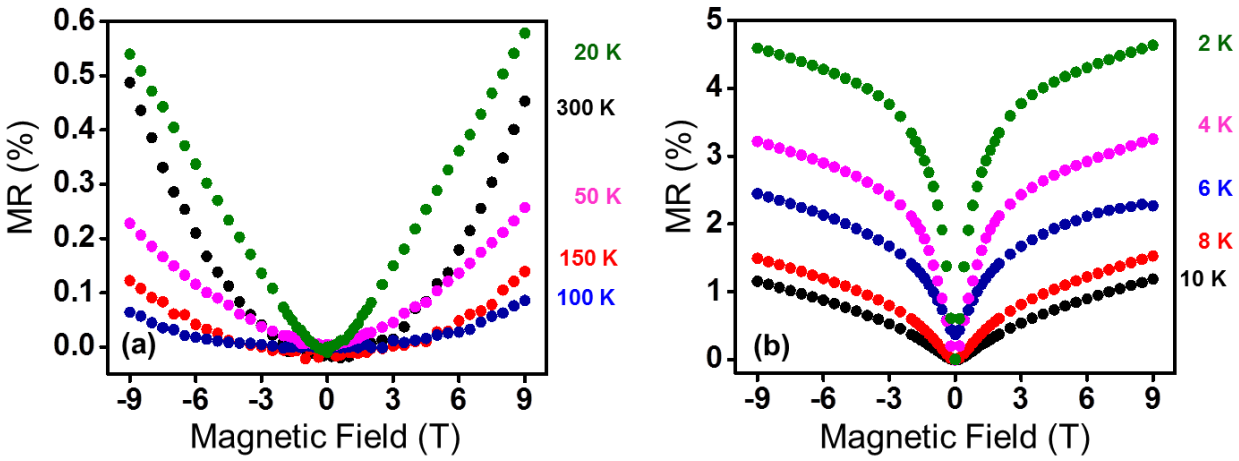

Figure 4.1 Magnetoresistance vs field curves of w38/t25 Bi anti-dot film at various temperatures; (a) from 300 K to 20 K, (b) from 10 K to 2 K.

At high temperatures (T >20 K, Figure 4.1 (a)), the MR curves showed parabolic shape without saturation up to 9 T, which is a typical feature seen in classical MR phenomena. On the contrary, below 10 K, MR sharply increased at low H and tended to saturate at higher H (Fig. 4.1 (b)). These results indicate that the film was out of the classical regime and that the WAL effect became dominant [2]. This behavior was also observed in the 35 nm-thick film and 50 nm-thick film on w = 30 nm templates, ((w48/t35) and (w57/t50), respectively) as well as the 25 nm-thick film on the w_{AAO}= 60 nm template (w76/t25) in Figure 4.2. From comparison of MR results in (w38/t25), (w48/t35), (w57/t50) and (w76/t25), it is evident that WAL effects were more enhanced in Bi anti-dot thin films of (w38/t25) at low temperature at low magnetic field areas. In addition, the graph shapes show similar behaviors over 8 K. The obtained magnetoresistance data between 4 K to 8 K were further subjected to detailed analyses to determine the dimensionality of the electron systems.

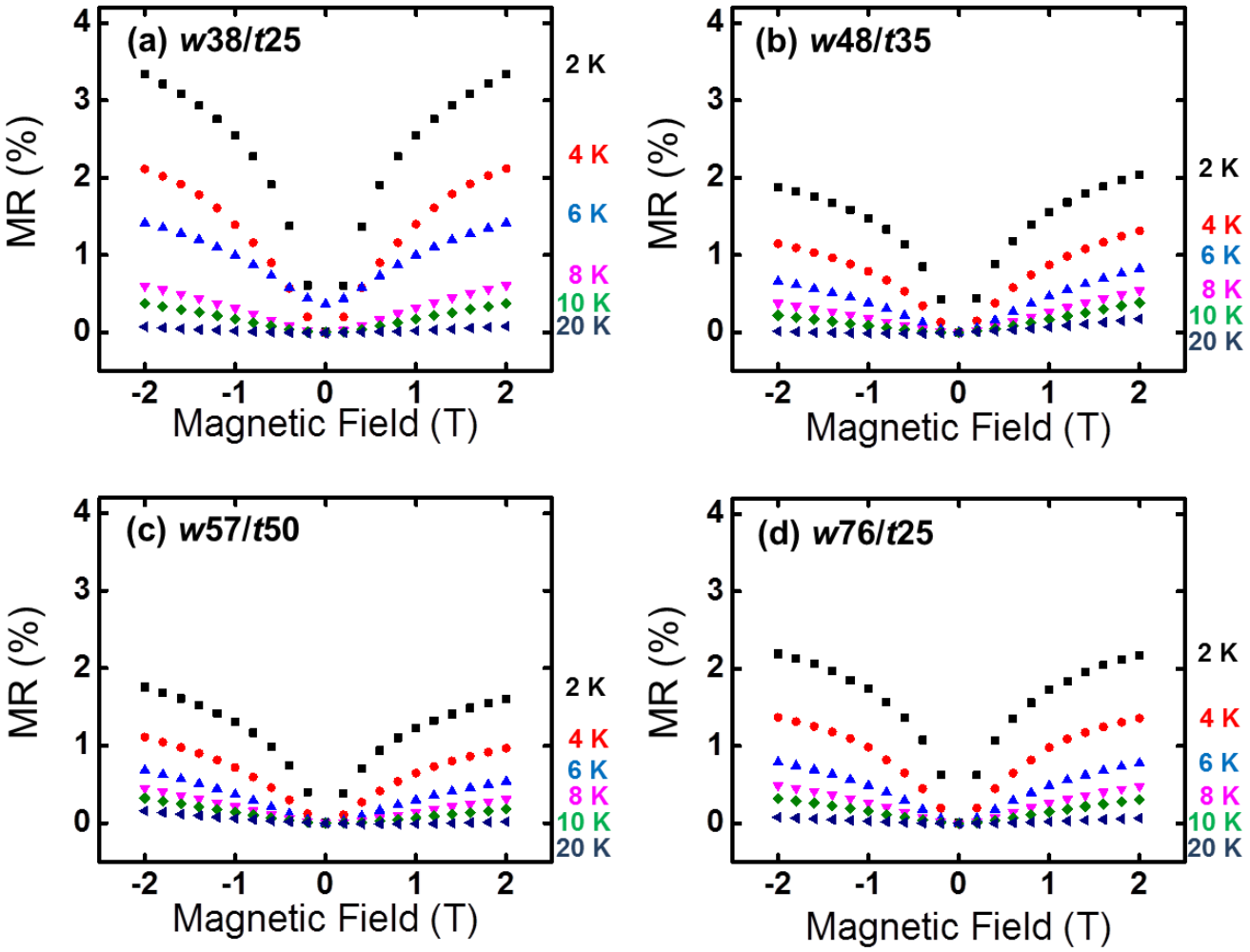

Figure 4.2 Magnetoresistance vs field curves of Bi anti-dot film from 20 K to 0 K; (a) *w*38/*t*25, (b) *w*48/*t*35, (c) *w*57/*t*50 and (d) *w*76/*t*25.

4.2 Dimensional crossover of tailored Bi anti-dot thin films

The quantum interference which includes information of electron-electron scattering interaction and electron localization is important in low dimensional systems. However, it is hard to describe these effects due to the conductivity vanishing by external magnetic field as well as very weak scattering. Therefore, to specifically investigate low dimensional electron behavior in Bi anti-dot structure, I used the Hikami-Larkin-Nagaoka (HLN) model [1].MR data was quantitatively analyzed by using 2D localization theory based on the HLN model, the WAL effect can be described by the following expression.

$$\Delta G_{sheet}(H) = \alpha \frac{e^2}{2\pi^2 \hbar} \times \left[\psi\left(\frac{1}{2} + \frac{H_\emptyset}{H}\right) - ln\left(\frac{H_\emptyset}{H}\right)\right], \quad (1)$$

where ΔG_{sheet} is the quantum correction to the sheet conductance ($\Delta G_{\text{sheet}}(H) = G_{\text{sheet}}(H) - G_{\text{sheet}}(0)$),$\alpha$ is a prefactor, ψ denotes the Digamma function and $H_\phi = \hbar/4eL_\phi^2$, where L_ϕ is the coherence length. According to the HLN model, α is −0.5 when the spin-orbit interaction is strong.

Figure 4.3 plots experimentally observed ΔG_{sheet}–H curves in the low field (0−2 T), low temperature (2−10 K) region (triangles). The figure also includes the results of curve-fitting assuming Eq. (1) (solid curves).The fitted curves well reproduce the experimental data, validating that Eq. (1), originally introduced to formulate the WAL effect in 2D electron systems, can be used even for 1D and 3D systems, as discussed later. The obtainedα values at 2 K were −0.63 for (*w*38/*t*25), −0.53 for (*w*48/*t*35), −0.57 for (*w*57/*t*50), and −0.5 for (*w*76/*t*25). This

indicates that electron transport in the present Bi anti-dots was significantly affected by strong spin-orbit interaction.

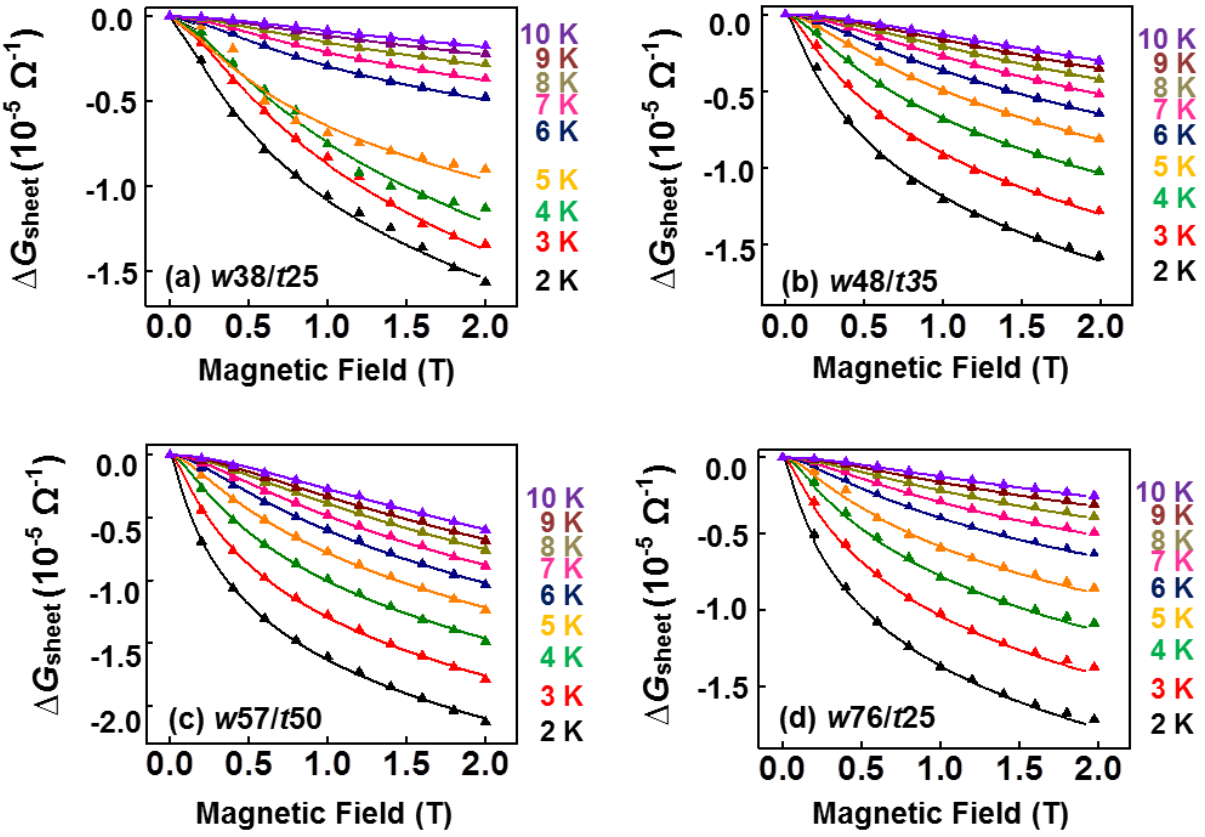

Figure 4.3 Magnetic field dependences of the sheet conductance of Bi anti-dot films at various temperatures; (a) *w*38/*t*25, (b) *w*48/*t*35, (c) *w*57/*t*50 and (d) *w*76/*t*25. The solid lines are the results of curve fitting assuming HLN model.

Figure 4.4 plots the values evaluated from the curve-fitting as function of T. L_ϕ is known to be expressed by a power law function of temperature (T), $L_\phi \propto T^{-b}$, where the power law factor is a measure of dimensionality: b = 1/3, 1/2 and 3/4 for 1D, 2D and 3D electron systems, respectively [3]. Indeed, the log-log plots in Figure 4.4 confirm this power law relationship. Notably, the (w38/t25) film exhibited a clear inflection point around T = 5 K. Below 5 K, b was estimated to be 0.46, indicating that the Bi anti-dot film had intermediate dimensionality between 1D and 2D (hereafter referred to as 1D−2D). In this film, the average values of both w_{Bi} and t were shorter than λ_F. However, w_{Bi} was distributed from 20 nm to 60 nm, as shown in Fig. 3.7, and the $w_{Bi}>\lambda_F$ components may have contributed to the 2D nature. Above 5 K, meanwhile, b was as high as 0.83, which is appreciated as 3D. The value of L_ϕ at the inflection point was ~38 nm, which is close to t or w_{Bi}. Thus, this phenomenon can be accounted for by dimensional crossover: the system undergoes 1D−2D to 3D dimensional crossover when L_ϕ becomes smaller than the anti-dot size. The (w48/t25) film also showed a weak inflection at T = 4−5 K (L_ϕ = 40−50 nm). The b values were 0.66 and 0.87 at T< 4 K and T> 4 K, respectively; indicating that 2D−3D to 3D crossover took place. Although the (w_{Bi}76/t25) film should show 2D behavior below ~8 K, where the film thickness t is shorter than both L_ϕ and λ_F, the L_ϕ –T relation in Figure 4.4(d) can be described by a single power curve with b = 0.82. This may be due to the inhomogeneity in film thickness. The (w57/t60) film with w_{Bi}, $t>\lambda_F$ showed 3D behavior (b = 1.0) down to 2 K. These results suggest that the 1D character may emerge when $w_{Bi}<L_\phi$ and w_{Bi}, $t<\lambda_F$.

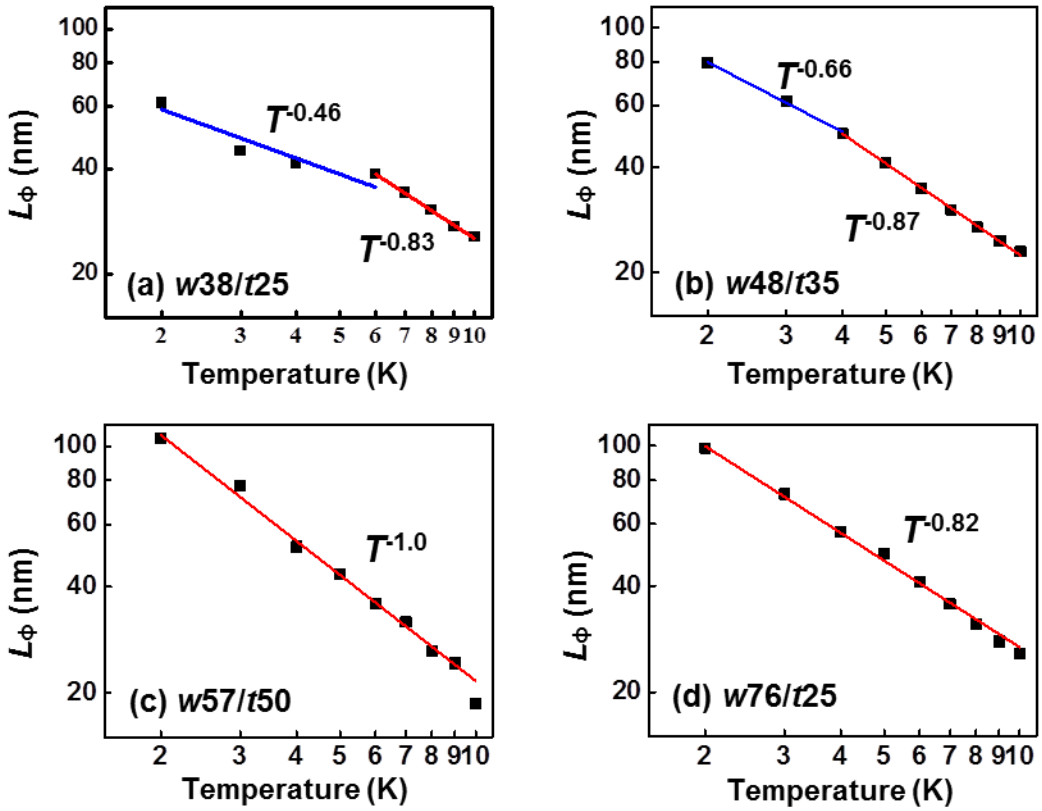

Figure 4.4Temperature dependences of L_ϕ evaluated from magnetoresistance data in Figure4.3. The solid lines are the results of power-low fitting.

A scenario to explain this inflection is that 1D−2D to 3D dimensional crossover occurs when L_ϕ falls shorter than the dimensions of the anti-dot structure. Such a dimensional crossover was previously reported for a submicrometer-sized Hall bar made of Bi_2Se_3 thin films [4]. The 20 nm-thick Bi_2Se_3 film showed 1D behavior below ~15 K, at which L_ϕ exceeded the width of the Hall bar (260 nm). Another possible mechanism to cause an inflection of L_ϕ is a change in the dominant inelastic scattering processes. Sangiao et al. [5] reported that 10 nm-thick Bi films showed an inflection at 1.5 K, below which inelastic surface scattering becomes dominant instead of electron-electron scattering. We think that the former mechanism is more plausible because (1) the inflection occurred at the temperature where L_ϕ exceeds w_{Bi} and (2) the (w76/t25) film, which had almost the same surface/volume ratio as that of the (w38/t25) film, showed no inflection.

References

1. S. Hikami, A. I. Larkin, and Y. Nagaoka, Prog. Theor. Phys. **63**, 707 (1980).
2. J. J. Lin and J. P. Bird, J. Phys.: Condens. Matter **14**, R501 (2002).
3. B. L. Altshuler, A. G. Aronov, and D. E. Khmelmitsky, J. Phys. C **15**, 7367 (1982).
4. S. Matsuo, T. Koyama, K. Shimamura, T. Arakawa, Y. Nishihara, D. Chiba, K. Kobayashi, T. Ono, C. Chang, K. He, X. Ma, and Q. Xue, Phys. Rev. B **85**, 075440 (2012).
5. M. Dyakonov and M. Shur, Phys. Rev. Lett. **71**, 2465 (1993).

Chapter 5

Magnetotransport properties of Bi anti-dot thin films

Bi is a famous semimetal material. In bulk Bi, the densities of carrier electron (*n*) and hole (*p*) are nearly equivalent. Meanwhile, in case of low-dimensional Bi, such as thin films and nanowires, *n* and *p* generally differs from each other [1-5], depending on temperature, due to the quantum confinement effect. For example, Marcano*et al*. reported that the carrier type of 300 nm-thick polycrystalline Bi thin films changes depending on the grain size of the film [4]. They also found that the transport properties of polycrystalline Bi films thinner than the Fermi wavelength (30 nm) show large contribution of carrier electrons from surface states [5]. On the other hand, such a variation of carrier type could not been studied in Bi nanowires because of the difficulty in Hall measurements. This motivated me to study magneto-transport properties of Bi anti-dot thin films, which have sizes smaller than the Fermi wavelength as well as the larger surface area to volume ratio comparable to Bi nanowires.

5.1 Fitting of two-band model

According to the two-band model [6], the longitudinal resistivity, ρ, and transverse resistivity (or Hall resistivity, ρ_{Hall}) can be described as

$$\rho = \frac{\rho_e\rho_h(\rho_h+\rho_e)+(\rho_e R_h^2+\rho_h R_e^2)H^2}{(\rho_e+\rho_h)^2+(R_e+R_h)^2H^2} \tag{5.1}$$

$$\rho_{Hall} = \frac{R_eR_h(R_e+R_h)H^3+(R_e\rho_h^2+R_h\rho_e^2)H}{(\rho_e+\rho_h)^2+(R_e+R_h)^2H^2} \tag{5.2}$$

where ρ_{e} and $\rho_{\mathrm{h}}$are the resistivity values of electron and hole, respectively, R_{e}=-1/qn and R_{h}=1/qp are Hall coefficients for electron and hole, respectively, and H is the applied magnetic field. Fitting Eqs. (5.1) and (5.2) to experimental ρ and ρ_{Hall} as functions of H yields the parameters ρ_{e},ρ_{h}, R_{e} and R_{h}, from which the n and p values and the motilities of electron and hole can be calculated.

Since H dependence of ρ originates only from Lorentz force in the two-band model, another mechanism causing H-dependent ρ, such as WAL, prevent the reliable analysis using the two-band model. Therefore, I have performed the fitting procedure for the magneto-transport data only above 50 K, at which WAL does not occur. For investigating the behavior of carriers in Bi anti-dot films as influenced by large surface to volume ratio and quantum confinement effect, magneto-transport measurements were conducted for the specimens, *w*38/*t*25, *w*57/*t*50, *w*73/*t*100 and *w*76/*t*25.

In Bi thin films, surface effect becomes dominant and surface current substantially contributes to the transport properties [5, 7]. The transport properties obtained by assuming the

two-band model are contributed by both bulk and surface carriers. Figure 5.1-4 plots ρ_{Hall}-H and ρ-H curves experimentally observed at 300 K, 150 K, 100 K and 50 K. The figure also includes the result of two-band model fitting (solid curves). The fitted curves well reproduce the experimental data at each temperature. For the*w*73/*t*100 film, only the data obtained at 300 K, 150 K and 100K will be discussed, because there is relatively large discrepancy between fitted curve and experimental data at 50 K.

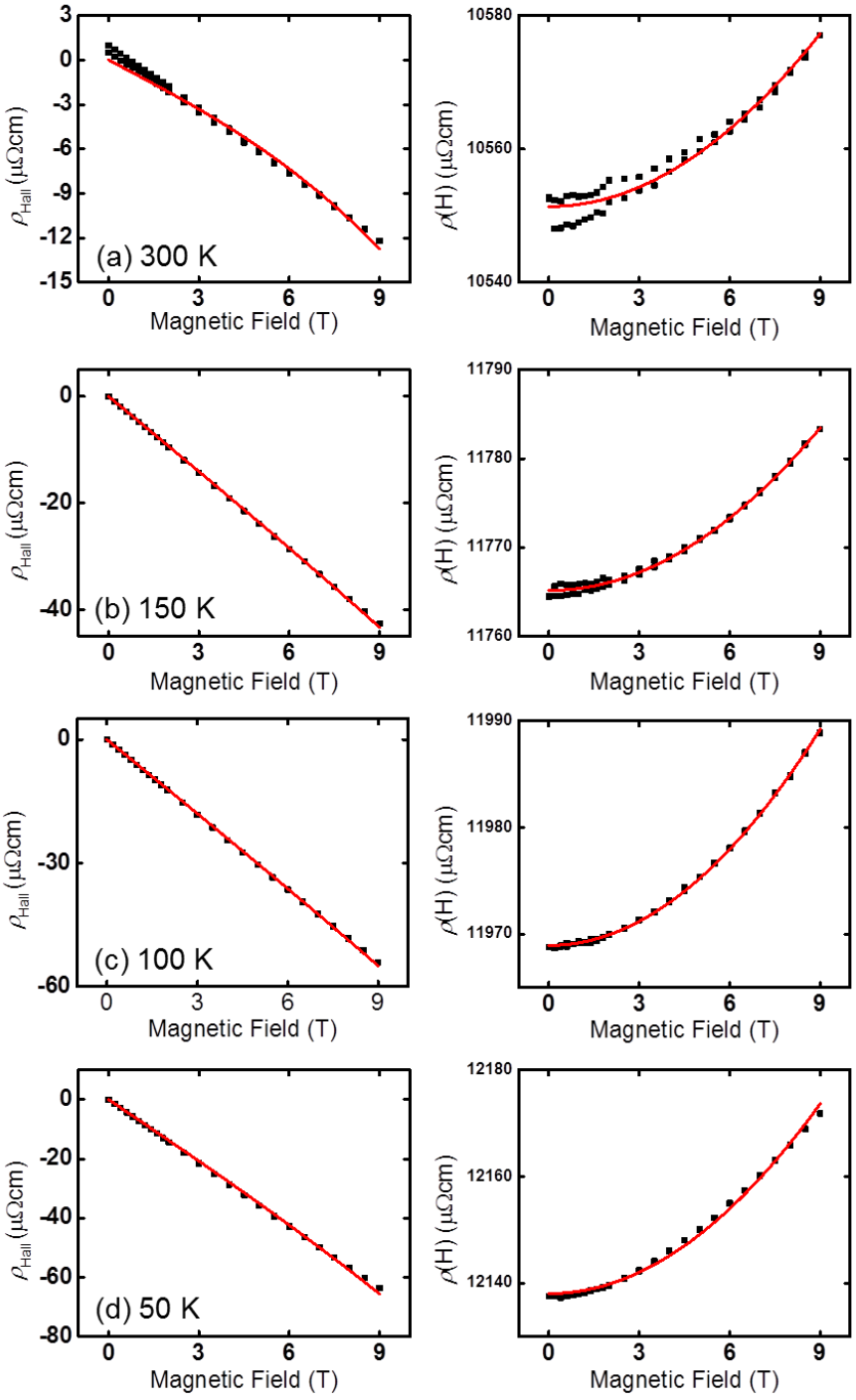

Figure 5.1 Hall resistance ρ_{Hall} (left) and resistivity ρ(right) of Bi anti-dot thin films functions of magnetic field at 300 K, 150 K, 100 K and 50 K. The pore wall width and the thickness of the film are 38 nm and 25 nm, respectively (w38/t25).

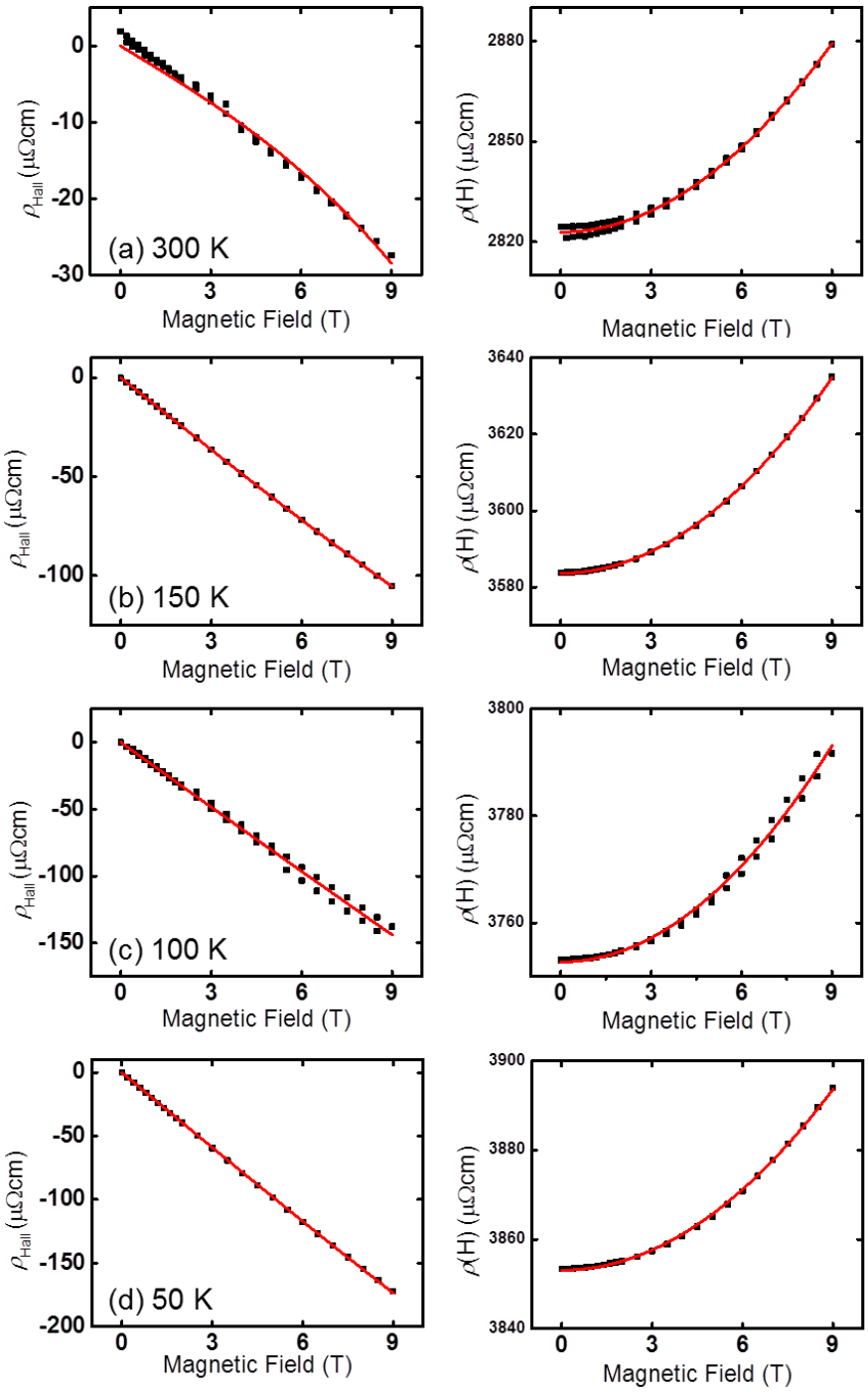

Figure 5.2 Hall resistance ρ_{Hall} (left) and resistivity ρ(right) of Bi anti-dot thin film as functions of magnetic field at 300 K, 150 K, 100 K and 50 K. The pore wall width and the thickness of the film are 57 nm and 50 nm, respectively (*w*57/*t*50).

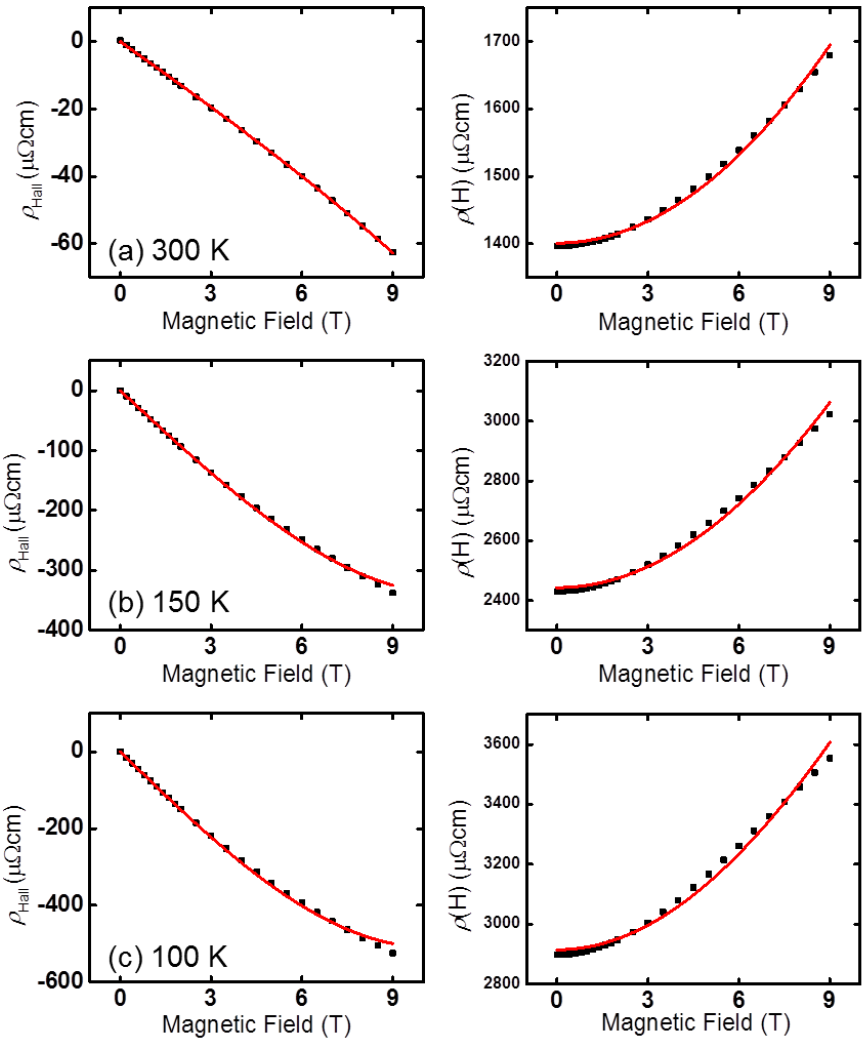

Figure 5.3 Hall resistance ρ_{Hall} (left) and resistivity ρ (right) of Bi anti-dot thin film as functions of magnetic field at 300 K, 150 K, and 100 K. The pore wall width and the thickness of the film are 73 nm and 100 nm, respectively (*w*73/*t*100).

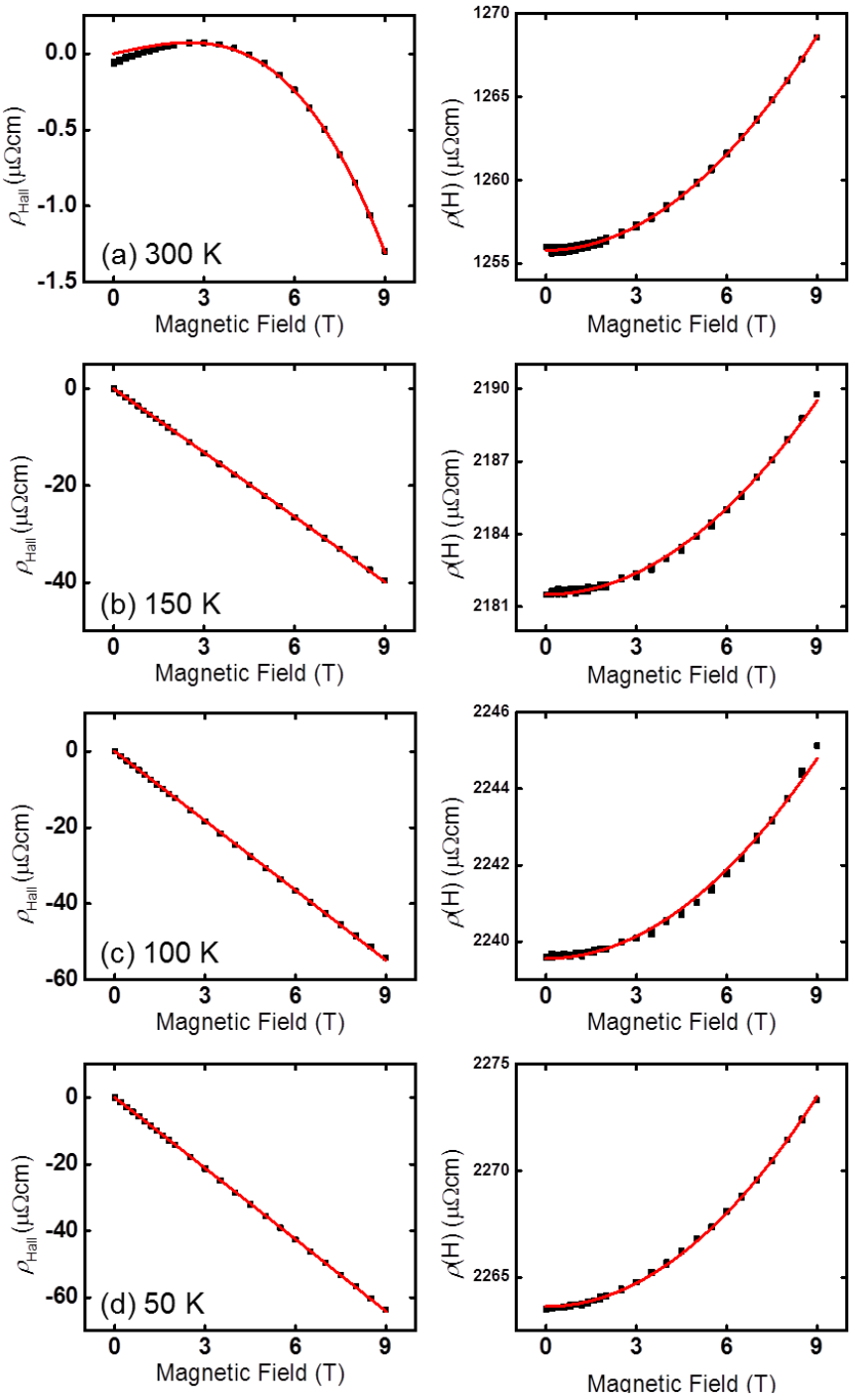

Figure 5.4 Hall resistance ρ_{Hall} (left) and resistivity ρ(right) of Bi anti-dot thin filmas functions of magnetic field at 300 K, 150 K, 100 K and 50 K.Thepore wall width and the thickness of the film are 76 nm and 25 nm (*w*76/*t*25).

5.2 Behavior of carriers in Bi anti-dot thin films

The carrier density of electron and hole, n and p, respectively, and the corresponding motilities, m_e and m_h, respectively, were calculate from the parameters estimated by the curve-fitting, ρ_e, ρ_h, R_e and R_h. The obtained carrier density and mobility values are shown in Figure 5.5 and Figure 5.6.

First, I discuss the film thickness (t) dependence of n and p for the w38/t25, w57/t50 and w73/t100 films, although w_{Bi} was also increased with t, despite the fact that the same AAO templates with w_{AAO}=30 nm were used, as described in the previous chapter. It is notable from that the majority carrier changed with respect to t. In the w73/t100 film, hole is dominant at 100 K and 150 K, while p and n are almost identical, p=4.2 $\times 10^{18}$ cm^{-3} and n=4.5 $\times 10^{18}$ cm^{-3}, respectively, at 300 K. In w57/t50, hole is still dominant below 150 K, but electron overwhelms hole at 300 K. In contrast, n is always higher than p at all the temperatures for w38/t25. This implies that the surface transport is dominated by electrons.

This tendency is more clearly seen from Figure 5.7, which plots n and p at various t against temperature. That is, n is gradually reduced with increasing t (Figure 5.7 (a)). Whereas, p revealed more complicated behavior (Figure 5.7 (b)), as follows. At 300 K, p is evaluated to be 5.4 $\times 10^{18}$ cm^{-3} for w76/t25, 2.7 $\times 10^{18}$ cm^{-3} for w57/t50 and 4.2 $\times 10^{18}$ cm^{-3} for w73/t100. These values are in the same order, except for 4.3 $\times 10^{17}$ cm^{-3}of$w$38/t25. The temperature dependence of p is quite similar between w76/t25 and w73/t100, which have the largest pore wall width in this experiment. The w38/t25 film shows a lower p value and p of w57/t50 maintains the temperature range 300 K to 50 K.

Next, I focus on the thinnest films, *w*38/*t*25 and *w*76/*t*25, of which thickness is shorter than the Fermi wavelength. As mentioned in the previous chapter, the former has dimensionality of 1D-2D, while the latter 2D/3D. Interestingly, electron is a major carrier in the *w*38/*t*25 film, similar to planar Bi film thinner than Fermi wavelength [5]. On the other hand, *p* of *w*76/*t*25 is about one order of magnitude larger than that of *w*38/*t*25. This increase of *p* cannot be understood by the analogy to the result of planar film [5] and might be attributable to the low dimensionality of anti-dot films, although it is unknown how dimensionality modifies the electronic structure of Bi. The electron and hole motilities showed the different behavior: m_e is obviously enhanced in *w*76/*t*25, while the m_h values are almost unchanged with *w*.

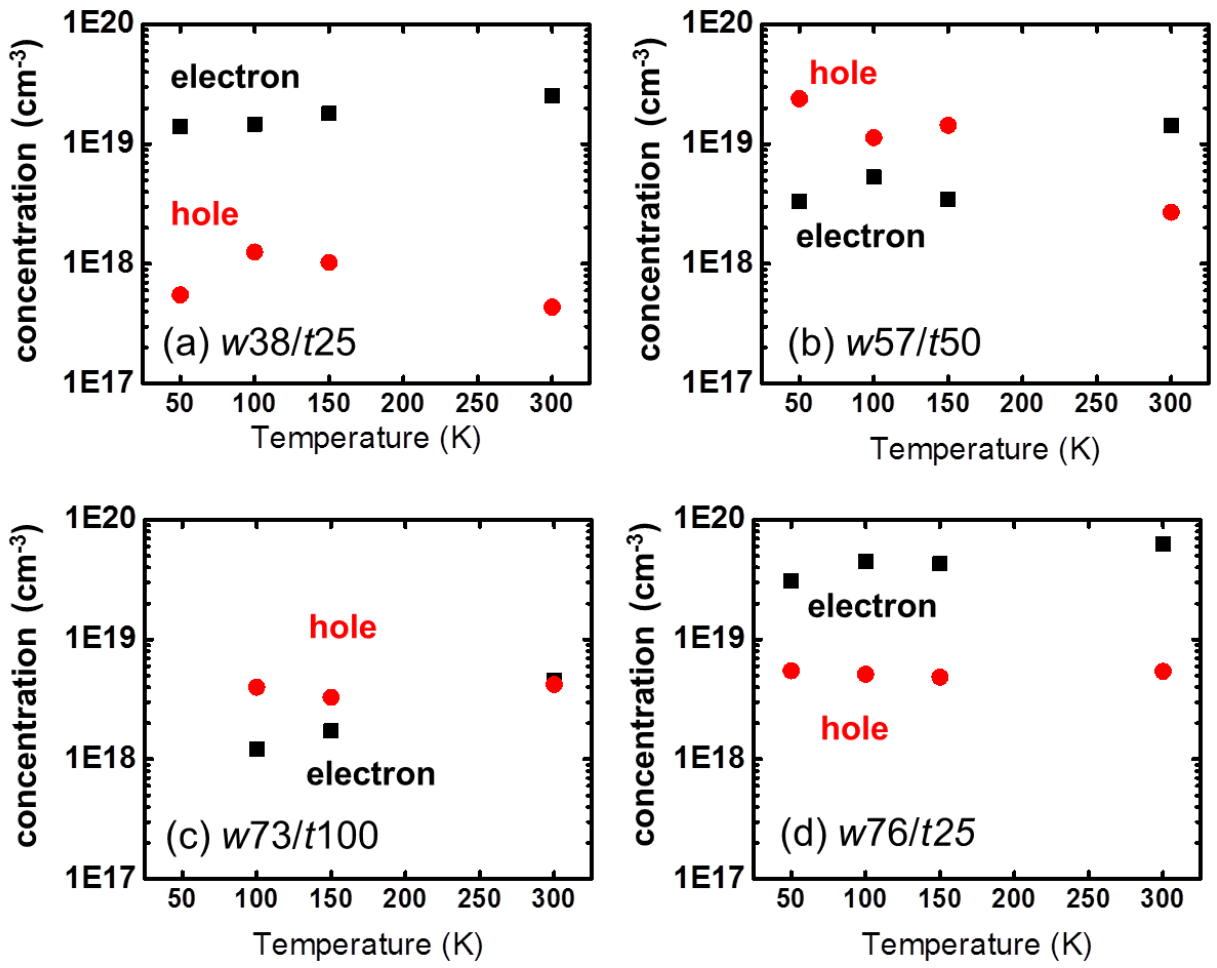

Figure 5.5 Carrier concentration estimatedby assuming two-band model. (a)*w*38/*t*25, (b)*w*57/*t*50, (c)*w*73/t100 and (d)*w*76/t25.

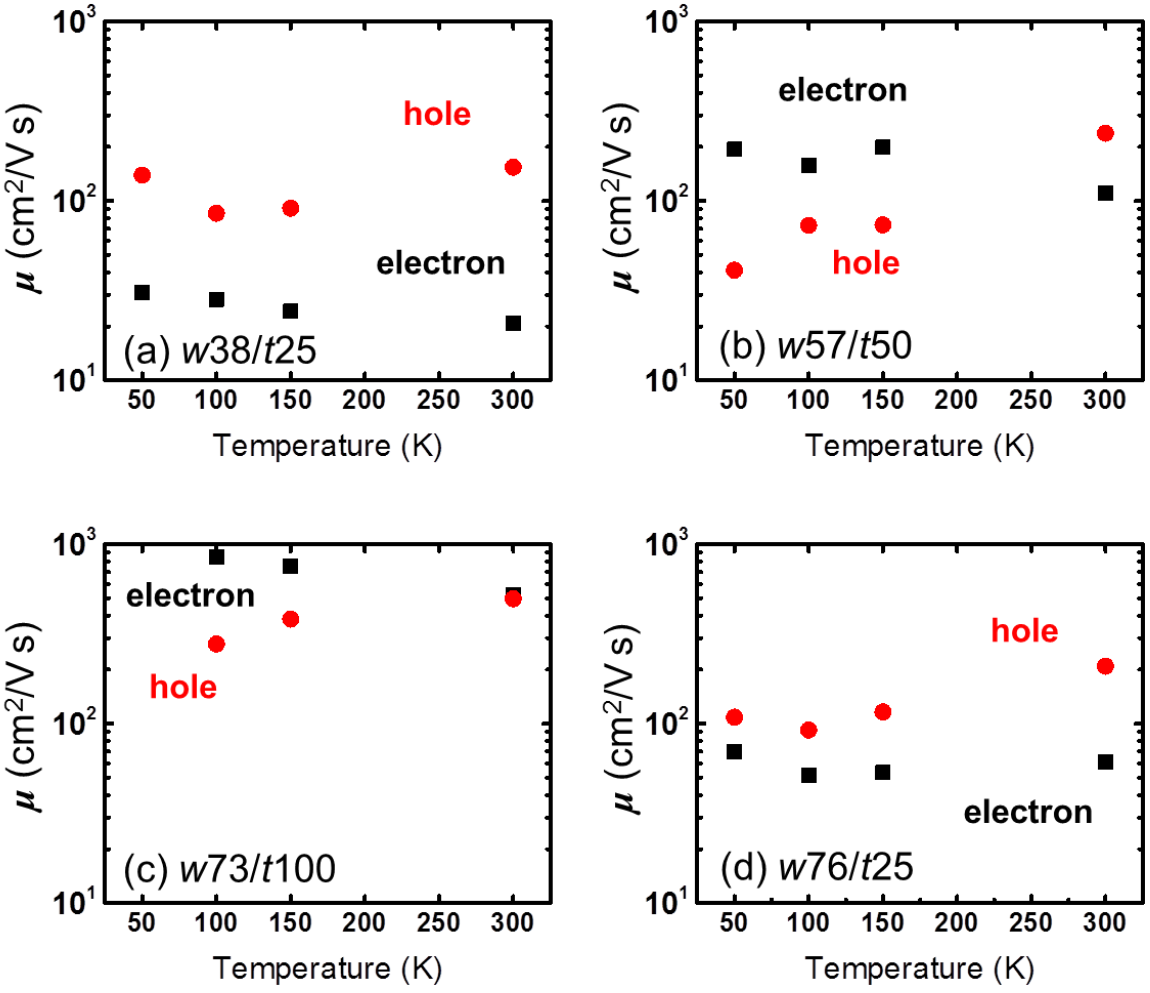

Figure 5.6 Mobility estimated by assuming two-band model. (a)*w*38/*t*25, (b)*w*57/*t*50, (c)*w*73/t100 and (d)*w*76/t25.

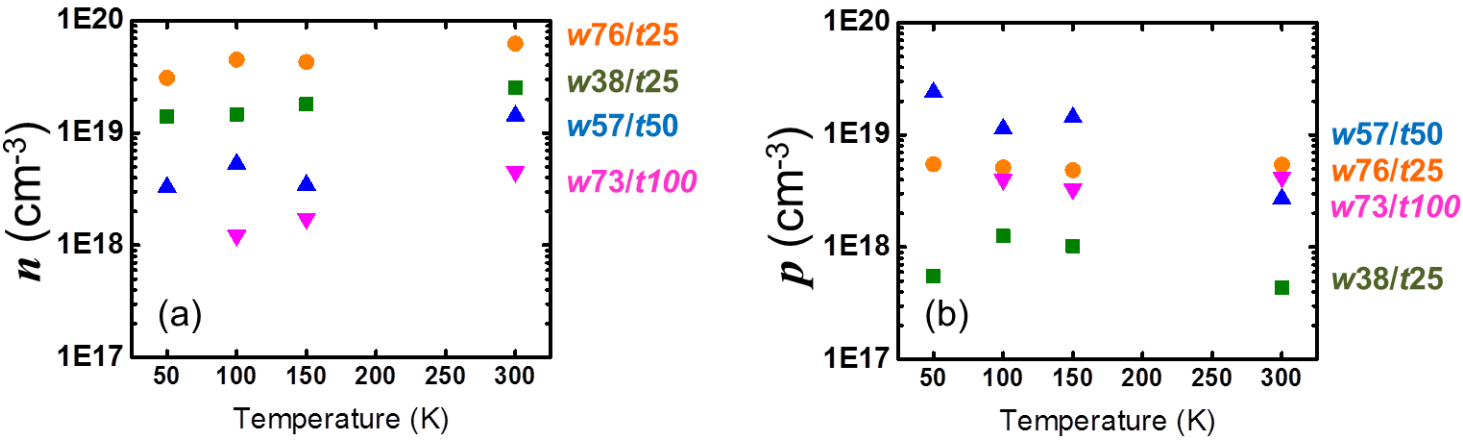

Figure 5.7 Temperature depends on *n* (a) and *p* (b) for Bi anti-dot thin films with *w*38/*t*25, *w*57/*t*50, *w*73/*t*100 and *w*76/*t*25.

References

1. M. Inoue, Y. Tamaki and H. Yagi, J. Appl. Phys. 45, 1562 (1974).
2. H. T. Chu, P. N. Henriksen, J. Jing, H. Wang and X. Xu, Phys. Rev. B **45**, 11233 (1992).
3. C. A. Hoffman, J. R. Meyer and F. J. Bartoli, Phys. Rev. B **48**, 11431 (1993).
4. N. Marcano, S. Sangiao, J. M. De Teresa, L. Morellon, M. R. Ibarra, M. Plaza and L. Perez, J. Mag. Mag. Mater. **322**, 1460 (2010).
5. N. Marcano, S. Sangiao, C. Magen, L. Morellon, M. R. Ibarra, M. Plaza and L. Perez and J. M. De Teresa, Phys. Rev. B **82**, 125326 (2010).
6. N. W. Ashcroft, N. D. Nermin, *Solid State Phys.*, Holt, Rinehart and Winston, 1976.
7. C. A. Hoffman, J. R. Meyer and F. J. Bartoli, Phys. Rev. B 51, 5535 (1995).

Chapter 6

Conclusions and Future Directions

In order to precisely characterize the low dimensional physical properties of Bi anti-dot thin films, porous structures have to be constructed in a well-defined manner. Therefore, effect of Al surfaceon the porous alumina layer fabricated on it has been studied in this thesis. The cyclic deposition process suppressed the undulation of the surfaces and hillock-like grain growth. The present anodization process successfully provided smooth Al surfaces without local burning during anodization, and the obtained AAO was able to be served as templates with well-defined pore wall widths. Base on this AAO template, tailored Bi anti-dot structures were fabricated, which were suited for controlling the dimensionality of Bi anti-dot by tuning pore wall widths and film thickness.

The Bi anti-dot thin films of *w*38/*t*25, *w*48/*t*35, *w*57/*t*50 and *w*76/*t*25 exhibited the weak anti-localization effect at low temperature (T<10 K). To evaluate the dimensionality of the system, the coherence lengths L_ϕ was derived by assuming the HLN model. Power-law fitting to the L_ϕ vs temperature plots clearly revealed dimensional crossovers from 1D or 2D to 3D, as follows. The *w*38/*t*25 film in which both w_{Bi} and t were smaller than λ_F had intermediate dimensionality between 1D and 2D below 5 K, while, the*w*38/*t*25 film showed 3D behavior above 5 K. The *w*48/*t*35 film also underwent dimensional crossover from 2D-3D to 3D around 4 K. The *w*57/*t*50 and *w*76/*t*25 films revealed 3D behavior down to 2 K. These results suggest that 1D character appear when both w_{Bi} and t were smaller than λ_F.

The transport properties, such as carrier densities and motilities, could also be influenced by the dimensionality of anti-dot structure. Assuming the two-band model, the densities of electron and hole were deduced independently. The electron density was substantially enhanced with decreasing the thickness of Bi anti-dot thin films, indicating that the surface carriers were dominated by electrons. In case of hole density, more complicated behavior was encountered. In the thinnest films with t = 25 nm, the hole carrier density was significantly increased with w_{Bi}, which might be related to the increase of dimensionality.

The present study demonstrated that anti-dot structures were useful not only for studying quantum confinement effects in low dimensional Bi but also for pursuing distinctive physical properties, such as infrared and THz spectral tuned by the size of anti-dots and enhanced thermoelectric effects originating from the unique network of low-dimensional conduction paths.

However, even in the 25-nm thick film, which was the thinnest examined here, clear 1D nature was not observed. One possible reason is that t and, particularly, w_{Bi}, were not enough smaller than the Fermi wavelength. To overcome this problem, it is needed to fabricate AAO template with much smaller w_{AAO} by conducting long time pore widening process. Moreover, the Bi film deposited on the AAO template must be much thinner. There is a difficulty in fabricating thinner Bi film, because the surfaces of Bi films are easily oxidized. In this experiment, I had to expose the Bi film deposited in the vacuum chamber in air for a short while, before the transport measurements. One idea to avoid the oxidization of Bi films is to do the sample transfer and setting process in a sufficiently inert atmosphere, for example, with the aid of portable vacuum chamber and glove box.

Another reason for the mixing of 1D and 2D seems to be the distribution of film thickness owing to the roughness of AAO template. Indeed, the roughness of the present AAO template made of Al thin film is larger than that of AAO made of Al foil. In this study, I used cyclic sputtering method to minimize the roughness of Al thin film. Further optimization of sputtering conditions may lead to the improvement of the surface roughness. Lowering temperature or use of dc sputtering is thought to be effective to suppress the grain growth and to make the film flatter.

If the Bi anti-dot film with smaller t and w_{Bi} can be deposited on smoother AAO template, 1D character will manifest itself more evidently. Additionally, the band structure of 1D Bi is interesting. The 1D anti-dot film will be the best specimen for directly investigating the band structure with spectroscopic methods.